ChemInform Abstract: Kinetics and Mechanisms of Aggregative Nanocrystal Growth

4 AUTHORS, INCLUDING:

Fudong Wang
Washington University in St. Louis
37 PUBLICATIONS **1,199** CITATIONS

Vernal Richards
Washington University in St. Louis
**8** PUBLICATIONS **214** CITATIONS

Kinetics and Mechanisms of Aggregative Nanocrystal Growth

Fudong Wang,* Vernal N. Richards, Shawn P. Shields, and William E. Buhro*

Department of Chemistry, Washington University, Saint Louis, Missouri 63130-4899, United States

ABSTRACT: The aggregative growth and oriented attachment of nanocrystals and nanoparticles are reviewed, and they are contrasted to classical LaMer nucleation and growth, and to Ostwald ripening. Kinetic and mechanistic models are presented, and experiments directly observing aggregative growth and oriented attachment are summarized. Aggregative growth is described as a nonclassical nucleation and growth process. The concept of a nucleation function is introduced, and approximated with a Gaussian form. The height (Γ_{max}) and width (Δt_n) of the nucleation function are systematically varied by conditions that influence the colloidal stability of the small, primary nanocrystals participating in aggregative growth. The nucleation parameters Γ_{max} and Δt_n correlate with the final nanocrystal mean size and size distribution, affording a potential means of achieving nucleation control in nanocrystal synthesis.

KEYWORDS: *nanocrystal, nucleation, growth, kinetics, mechanism, aggregation, coalescence*
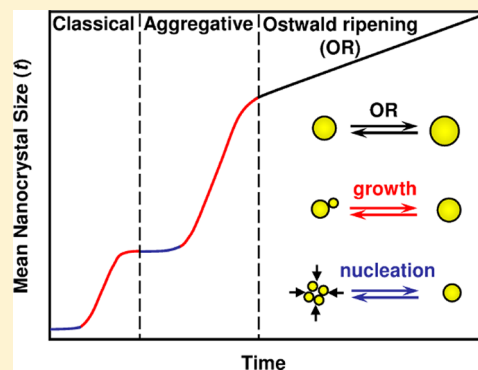
1. INTRODUCTION

A hundred years ago, synthesis in organic chemistry was an empirical enterprise guided largely by chance experimentation, which had resulted in a catalog of useful but poorly understood procedures. Early in the 20th century, the mechanisms governing organic transformations, such as those for aliphatic (S_N1, S_N2)[1,2] and aromatic substitution,[3,4] were elucidated, putting bond-forming reactions on a systematic basis. The tremendous sophistication of organic synthesis today is largely due to the development of mechanistic understanding, and the resulting availability of a set of widely accepted mechanisms.

Christopher Ingold, a major early contributor to mechanistic organic chemistry, astutely foreshadowed the future development of organic synthesis in the following statement:[5,6]

> "The new work made it inescapably clear that the old order in organic chemistry was changing, the art of the subject diminishing, its science increasing: no longer could one just mix things: sophistication in physical chemistry was the base from which all chemists, including the organic chemist, must start."

In our view, the current state of nanocrystal synthesis is comparable to that of organic synthesis a century ago. Empirical procedures have been developed for the preparation of a wide range of semiconductor, ceramic, and metallic nanocrystals. In many cases, the procedures have been optimized to provide narrow nanocrystal size distributions and control over mean sizes. However, the work is more empirical art than science. Nanocrystal synthesis is not far beyond the "eye of newt and toe of frog"[7] stage. Mechanisms are sometimes invoked without evidence, and, until fairly recently, little experimental mechanistic work had been completed. Apart from the classical LaMer mechanism[8-18] and Ostwald ripening,[19-34] a set of varied and widely accepted growth mechanisms to purposefully guide nanocrystal synthesis is not yet available.

Studies of the formation mechanism of colloidal gold date back to 1951.[35] However, the modern era for mechanistic studies of nanocrystal growth appear to have begun in the mid-1990s.[36] Most experimental studies of nanocrystal growth and size focusing have invoked the LaMer mechanism,[12-18] Ostwald ripening,[21-34] or their combination.[37-40] The principal feature of the LaMer mechanism is that nucleation is temporally confined to an early burst period. In Ostwald ripening, larger nanocrystals grow at the expense of smaller nanocrystals, which are progressively dissolved. Finke and co-workers have published a series of experimental papers in which continuous nucleation and autocatalytic growth are proposed.[41-43] Several experimental mechanistic studies have identified the participation of nanocrystal aggregation and coalescence in growth processes.[44-68] Some mechanistic work is not readily categorized.[69,70] Important theoretical studies of nanocrystal nucleation and growth have been contributed by Jensen and Bawendi,[71] Matijević,[51,72] Mulvaney,[73] Peng,[69] Privman,[74,75] Skrdla,[76-78] Talapin,[31] Zukoski,[55,57,79] and others.[80]

The contribution of aggregative processes to the growth of colloidal particles was recognized very early. Uyeda and co-workers determined the multiply twinned internal structures of gold nanoparticles in 1973,[81] which they proposed to result from coalescence of initially formed primary particles prior to particle growth. At approximately the same time, a reinvestigation of the classical LaMer growth of sulfur sols

demonstrated that particle number densities passed through a maximum early in the growth process and then declined in time.[82] This decrease was attributed to particle coalescence. Subsequently, colloidal particles of various well-defined shapes were observed to be composed of smaller, primary nanocrystallites having diameters of 1−3 nm, indicative of aggregation.[48,83] In the 1990s, Zukoski and co-workers began to incorporate aggregative processes into their kinetic schemes for the growth of gold, silver, and silica nanoparticles.[36,55,57] Later, Finke and co-workers incorporated nanocluster agglomeration into their kinetic schemes as well.[45−47,49,50] Banfield and co-workers elucidated the oriented-attachment mechanism[56,58,59,84] of nanocrystal growth in 1998,[58] which is an aggregative process. More recently, nanocrystal growth by aggregation and coalescence has been directly observed in real time by in situ transmission electron microscopy (TEM) studies.[44,85−90]

In this review, we argue that advantages inherent in aggregative growth will potentially allow the systematic, rational control of nanocrystal size and size distribution to be achieved. In section 2, we summarize the conditions necessary to achieve such control, and we introduce the concept of a nucleation function. In section 3, we review the exciting recent developments in the direct observation of aggregative growth. Section 4 addresses the kinetics of aggregative growth. Section 5 reviews the experimental determination of aggregative nucleation functions, and their role in controlling nanocrystal sizes and size distributions. We hope to convince that mechanism-based synthetic control in nanocrystal synthesis is within reach.

2. STRATEGY FOR SIZE CONTROL

The classical picture for homogeneous nucleation and growth is summarized in the familiar plot from LaMer and Dinegar (see Figure 1).[10] The plot assumes a chemical reaction that
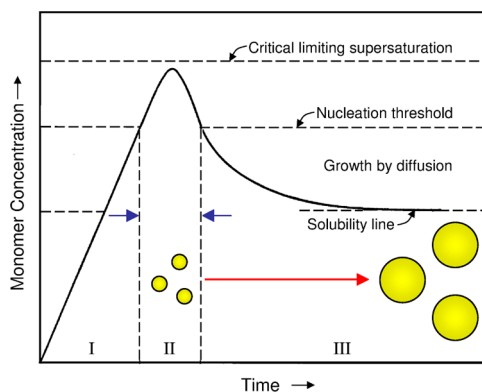

Figure 1. Schematic representation of monomer concentration during particle nucleation and growth from solution in a classical LaMer mechanism.[10] The blue arrows identify the nucleation period (zone II). The red arrow indicates the growth period (zone III).

produces a monomer, such that the monomer concentration steadily rises in time zone I, and passes the threshold concentration for nucleation in time-zone II. Nucleation and subsequent growth decreases the monomer concentration below the nucleation threshold, such that nucleation ceases and growth upon the existing nuclei occurs in time zone III. Consequently, nucleation is restricted to zone II, and, in the classical picture, the number of nuclei generated in this period

determines the number of growing particles. The time width of zone II determines the width of the resulting particle-size distribution.

The time-dependent nucleation rate, $\Gamma(t)$, parallels the monomer-concentration profile in zone II (Figure 1).[91] At the beginning of zone II, $\Gamma(t) = 0$. The nucleation rate subsequently rises, passes through a maximum, declines, and returns to zero at the end of zone II. We refer to this time-dependent behavior of the nucleation rate as the *nucleation function*.[92] Experimental nucleation functions have been measured in a few cases.[91−98] They are apparently asymmetric,[91] but they are reasonably well approximated by Gaussian functions.[92,99] Some schematic nucleation functions are depicted in Figure 2.
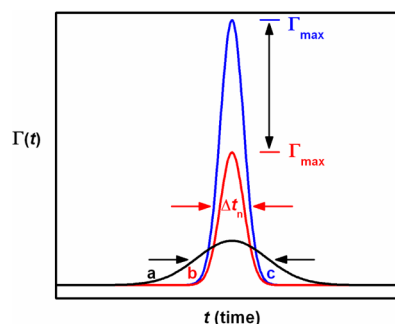

Figure 2. Three schematic nucleation functions a−c having Gaussian profiles (black curve, function a; red curve, function b; blue curve, function c). The width of the nucleation function (Δt_n) provides a measure of the time window for nucleation. The maximum nucleation rate is Γ_{max}. The area under the nucleation function is the number of particles nucleated (N). Reprinted with permission from ref 95. Copyright 2011, American Chemical Society, Washington, DC.

For a classical nucleation-and-growth process, the ultimate mean particle size and size distribution are encoded in the nucleation function. The 2σ width of the nucleation function (Δt_n) provides a measure of the time window for nucleation. Because Δt_n is smaller for function b than that for function a in Figure 2, the nucleation process described by function b will produce a narrower final particle size distribution.

The area under the nucleation function is N,[92] the number of nuclei formed. Functions b and c in Figure 2 have identical Δt_n values, and should produce equally narrow size distributions. However, function c has a larger maximum nucleation rate Γ_{max} and thus a larger under-curve area. Thus, with an equal number of monomers generated, the nucleation process described by function c will produce a larger N and ultimately a smaller final particle mean size.

The rational control of nanocrystal mean sizes and size distributions are arguably the two greatest challenges in nanocrystal synthesis. Gaining control of the nucleation function through purposeful manipulations of Δt_n and Γ_{max} provides a potential means of achieving those goals. Ideally, conditions would be found to minimize Δt_n, ensuring a narrow final size distribution. The number of nuclei N, and thus the final mean nanocrystal size, would be best controlled by variation of Γ_{max}, at the minimized value of Δt_n.

Achieving synthetic control by this nucleation-control strategy requires that nucleation functions be experimentally measurable, and that Δt_n and Γ_{max} be amenable to purposeful variation by chemical or other means. Indeed, critical-nucleus sizes in classical-nucleation processes have been determined to

be in the range of tens to hundreds of atoms or molecules, theoretically and experimentally.[100−116] This very small size scale is not readily accessible to experimental measurement; therefore, determination of time-dependent nucleation rates is challenging.

Nucleation functions and nucleation rates have been measured in several studies, particularly in the colloidal crystallization of polymer spheres[113] and in protein crystallization,[110−112] where the length and time scales are considerably larger than those for the classical nucleation of metals, semiconductors, ceramics, or small-molecule crystals. For colloidal and protein crystallization, nucleation rates have been experimentally determined by light scattering,[102,105,107,112,113] atomic force microscopy (AFM),[108,110] scanning tunneling microscopy (STM),[104,116] and by direct video microscopy.[111] In this review, we argue that aggregative nucleation and growth using small primary nanocrystals affords similar length-scale advantages and enables the experimental determination of nucleation functions under various conditions.

Aggregative nucleation and growth by necessity follows classical nucleation and growth. A general kinetic profile depicting the regimes of nanocrystal growth, with the participation of aggregative processes, is given in Figure 3. An
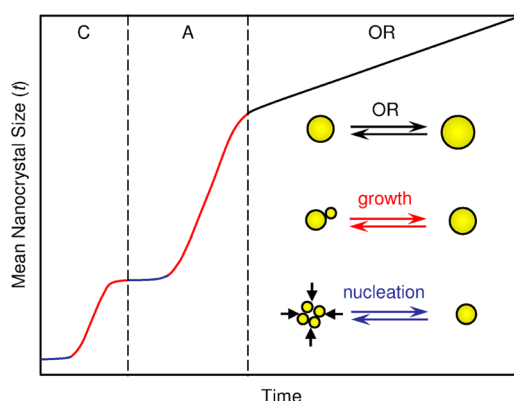

Figure 3. Schematic representation of nanocrystal growth including classical nucleation and growth (regime C), aggregative nucleation and growth (regime A), and Ostwald ripening (regime OR). The three regimes may overlap temporally to varying extents, which is not shown here. Nanocrystal nucleation, growth, and Ostwald ripening steps are color-coded in the sigmoidal (S-shaped) kinetic profile as blue, red, and black, respectively. The smallest yellow circles represent atoms, ions, molecules, or small clusters in regime C, and primary nanocrystals in regime A.

initial induction period and size increase correspond to classical nucleation and growth, respectively, in regime C (for "classical"). The classical regime may produce primary nanocrystallites, often in the diameter range of 1−3 nm. That regime *may be* followed by a second induction and growth period associated with aggregative nucleation and growth in regime designated as A (for "aggregative"). Ostwald ripening may occur in a final regime designated as OR (for "Ostwald ripening").

We note that the three regimes may overlap temporally to varying extents. The relative magnitudes of nanocrystal growth occurring in the classical and aggregative regimes may vary, or the aggregative regime may be absent. Ostwald ripening may also be absent. Nucleation functions are associated with both classical and aggregative nucleation, but the last active

nucleation process determines final nanocrystal sizes and size distributions.

As noted above, one also requires the means for purposeful variations of Δt_n and Γ_{max}, such that the height and width of the nucleation function may be controlled. For aggregative nucleation and growth from small primary nanocrystals, we have suggested that any additive that influences the colloidal stability of the nanocrystals may potentially vary the nucleation-rate behavior.[92,94,95] Indeed, nucleation rates in protein crystallization have been controlled in this manner.[110−112] In contrast, nucleation control in classical nucleation will require factors that influence the stability of monomer species consisting of a single to a few atoms, which are similar to reactive intermediates. They will not likely respond to polymer or ionic additives in the same manner as do primary nanocrystallites. Therefore, classical nucleation may be inherently more difficult to control, because the nucleation function is not as readily measured or manipulated. Nucleation control in nanocrystal growth by aggregative processes may be more readily achievable.

3. DIRECT OBSERVATION OF AGGREGATIVE GROWTH

Perhaps the most-exciting recent development in mechanistic understanding of colloidal-nanocrystal nucleation and growth is the real-time visualization of growth trajectories of individual nanocrystals in dispersion, using a liquid cell in a TEM. In the first such study, Alivisatos and co-workers observed that colloidal platinum nanoparticles grew both by simple monomer attachment in solution and by particle coalescence.[44] Fascinating details were revealed about the growth processes.

The study employed the precursor Pt(acetylacetonate)$_2$ in a solution containing an oleylamine surfactant. The electron beam in the TEM induced the nucleation of platinum nanocrystals, which continued for over 10 s, such that nanocrystal growth temporally overlapped the nucleation period. Nanocrystals grew by both monomer addition and coalescence events. The number of nucleated nanocrystals reached a maximum at 21 s, and then significantly declined to a constant value. Nanocrystal aggregation and coalescence was primarily responsible for this decline. The aggregative growth also produced the expected bimodal size distribution at 24 s, which later resolved into a sharpened single mode.

The rate behavior and other characteristics of the growth processes differed between the classical, monomer-addition, and aggregative-coalescence pathways.[44] Nanocrystals undergoing only monomer addition grew continuously until reaching a saturation size, maintaining nearly spherical morphologies (Figure 4). In addition, a near-constant, uniform diffraction contrast persisted in such nanocrystals throughout growth, indicating them to be single crystals.

In contrast, nanocrystal growth by aggregation and coalescence was discontinuous.[44] Obviously, such growth produced stepwise size increases, as nanocrystals of comparable dimensions were coalesced within a short time period. However, subsequent growth was observed to pause in an interval immediately following coalescence, both by monomer addition and further coalescence events. During this pause period, the coalesced particle was observed to rearrange in morphology, eventually achieving a near-spherical shape (Figure 4). Moreover, the diffraction contrast was observed to be uneven and to dynamically shift during the pause while a structural rearrangement and recrystallization process occurred,
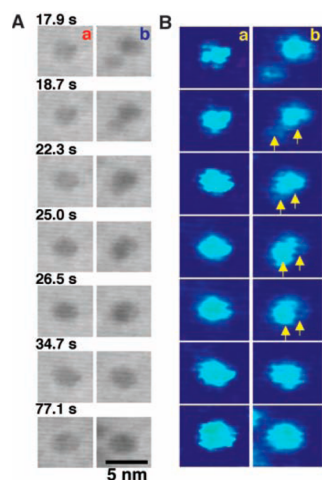
Figure 4. Comparison of different growth trajectories of colloidal platinum nanoparticles: (A) video images showing simple growth by means of monomer addition (a, left side of panel) or growth by means of coalescence (b, right side of panel); (B) enlarged (1.5×) color images of images shown in panel A. Distinct contrast changes in the coalesced particles are highlighted with arrows, indicating recrystallization. Reprinted with permission from ref 44. Copyright 2009, The American Association for the Advancement of Science, Washington, DC.

ultimately affording a single-crystalline nanoparticle. Smaller nanocrystals were found to be more prone to multiple coalescence events than were larger nanocrystals, which was attributed to their larger surface fractions and energies, and increased mobility and collision frequency.[44]

Subsequently, many research groups have reported the real-time monitoring of aggregative processes among colloidal nanoparticles by using in situ TEM. Grogan and co-workers observed the aggregation (but not coalescence) of gold nanoparticles, the kinetics of which were consistent with a diffusion-limited-aggregation model.[117] Similarly, Evans and co-workers monitored the growth of PbS nanoparticles, in which monomer-attachment, coalescence, and Ostwald-ripening processes were observed.[86] Mirkin and co-workers studied the dynamics of gold-nanoparticle coarsening in attoliter-volume reactors created by scanning-probe block-copolymer lithography, in which the coalescence process could be differentiated from Ostwald ripening.[85] Xin and Zheng studied the Ostwald ripening of bismuth nanoparticles under precursor-scarce conditions.[88] They revealed oscillating ripening behavior among pairs of adjacent nanoparticles, in which one grew at the expense of the other for a time, and then the process reversed. The growth of a small nanoparticle at the expense of a larger one was described as "anti-Ostwald ripening".

Lee, Zettl, Alivisatos, and co-workers obtained a higher-resolution observation of platinum-nanocrystal growth using liquid cells having graphene windows.[89] Such cells provided several advantages over the previously developed cells employing thicker, Si_3N_4 or SiO_2 windows.[44,86,118] This study revealed that the coalescence of platinum nanocrystals proceeded along a specific crystallographic orientation, corresponding to the fusion of {111} facets. The likely lowest ligand coverage for {111} planes due to their lowest surface energy (for a face-centered cubic crystal such as platinum) may facilitate nanocrystal contact at {111}. Before coalescing along the {111} orientation, the nanocrystals showed correlated rather than independent motion over a prolonged period to facilitate

lattice alignment. The correlated motion apparently rises from attractive forces, including van der Waals interactions.

After coalescence, the nanocrystals gradually reshaped and evolved truncated facets, exhibiting single-crystalline or twinned structures.[89] The single-crystalline structures resulted from the joining of mirror {111} facets, whereas the twinned structures resulted from the fusion of misoriented {111} facets. The twin boundaries so generated remained locked within the nanocrystals as they underwent morphological remodeling. Misoriented coalescence thus appears to be the origin of the twinned nanocrystals common for face-centered cubic (fcc) metals, as has been previously proposed.[81]

Zheng and co-workers studied Pt_3Fe nanorod growth in solution by in situ TEM, which proceeded in three stages.[90] In the first stage, monodisperse spherical nanoparticles grew by parallel monomer attachment and nanoparticle coalescence. In the second stage, the nanoparticles formed flexible nanoparticle chains as a result of dipolar interactions between nanoparticles. In the final stage, adjacent nanoparticles underwent fusion via initial neck formation, producing twisted polycrystalline rods. These twisted structures persisted over extended times prior to straightening into single-crystal nanorods. This straightening process was presumably driven by the decrease in total energy from reducing interfacial energy and eliminating crystal defects.

Parent and co-workers reported the in situ scanning tunneling electron microscopy (STEM) study of palladium nanoparticle synthesis in a liquid-crystal surfactant template. They observed that palladium nanoparticles grew through coalescence or sintering after small (~2−5 nm) spherical particles were nucleated.[87]

The in situ TEM-monitoring studies summarized in this section show clearly that nanocrystal aggregation and coalescence are general features of colloidal-nanocrystal growth.

4. KINETICS OF AGGREGATIVE GROWTH

The kinetics of diffusion-limited colloid aggregation (DLCA)[119−123] and reaction-limited colloid aggregation (RLCA)[124−131] have been studied since the early 1980s. In RLCA, a Smoluchowski rate equation,[55,132] describing the time-dependent evolution of the number density of particles as a function of size as they aggregate, is often used to represent the aggregation probability as a function of the masses of two colliding clusters or particles. In 1991, Bogush and Zukoski applied this model to the aggregative growth of primary silica nanoparticles 3−10 nm in diameter, showing that aggregation alone was capable of producing narrow size distributions in the resulting, larger, near-monodispersed colloidal spheres.[55] Their seminal work concluded that small, primary nanoparticles were colloidally unstable and rapidly aggregated at early times to achieve stable-size aggregates. The number of growing aggregates was set by this initial process. Subsequent growth occurred by addition of primary nanoparticles to these larger, stable aggregates. We argue here that the initial aggregation and subsequent stepwise addition constitute a nonclassical nucleation-and-growth mechanism.

Within the same decade, Matijević, Privman, and co-workers similarly demonstrated that the aggregation of primary particles was mechanistically capable of producing larger, monodispersed secondary colloids of gold.[51] Zukoski and co-workers subsequently extended their model to the aggregative growth of silver nanocrystals.[57] Kinetic studies of oriented attachment emerged in 2003.[52,56,60,133−136] Finke first reported a four-step mechanism combining classical and aggregative growth in

8

dx.doi.org/10.1021/cm402139r | *Chem. Mater.* 2014, 26, 5−21

2005.[45,46,49,50,63] Following these initial studies, the contribution of aggregative processes to nanocrystal growth, in certain cases, has been well-established (see below).

Kinetic studies of aggregative growth can be complicated by the temporal overlap of classical nucleation and growth, aggregative growth, and Ostwald ripening.[36,45,46,49,50,55,57,63,92,94,95] By studying the growth of small, preformed primary nanoparticles, classical nucleation and growth are removed from the mechanistic scheme. Then the kinetics and other mechanistic observations only need to distinguish between aggregative growth and Ostwald ripening. This approach is pursued in the following subsection.

4.1. Distinguishing Aggregative Growth and Ostwald Ripening. Our interest in aggregative growth was stimulated by two papers of Zhong and co-workers,[137,138] in which solvent dispersions of small (1.7 nm) thiolate-capped gold nanocrystals having broad size distributions were coarsened to larger nanocrystals having narrow size distributions. The authors claimed that growth occurred by a core coalescence, or aggregative, process. In contrast, we suspected that coarsening had occurred by Ostwald ripening, a conventionally accepted mechanism for the conversion of smaller-nanocrystal size populations into larger ones. We thus undertook a mechanism and kinetics study of the coarsening process.[92] Our findings concurred with the initial claim of Zhong and co-workers.

We measured the coarsening kinetics of 1.7-nm-diameter thiolate-capped gold nanocrystals by monitoring the mean nanocrystal size, expressed as the mean volume $\bar{V}(t)$, as a function of time. A typical kinetics curve is plotted in Figure 5,
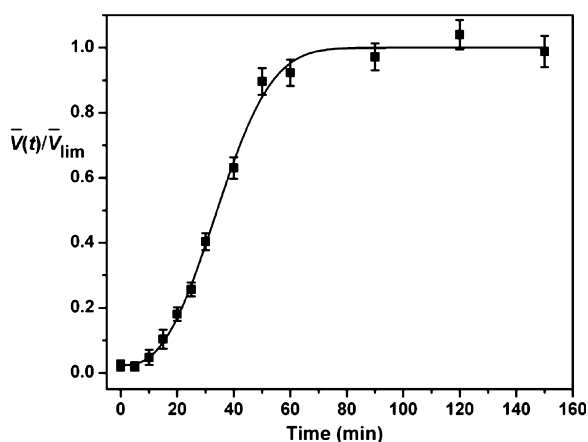

Figure 5. Sigmoidal coarsening kinetics and the fit of eq 1 (given later in the text) for 1.7-nm-diameter thiolate-capped gold nanocrystals. $\bar{V}(t)$ is the nanocrystal mean volume at time t, and $\bar{V}_{lim}$ is the final nanocrystal mean volume. Reprinted with permission from ref 92. Copyright 2010, American Chemical Society, Washington, DC.

which showed sigmoidal (S-shaped) coarsening kinetics. An initial induction period was followed by a regime of rapid growth, after which further growth was discontinued for a significant length of time.

Sigmoidal growth kinetics such as those depicted in Figure 5 are typically observed for classical LaMer nucleation and growth (regime C in Figure 3).[15,16,18,31,41−43] The initial induction period is attributed to the nucleation regime, in which a population of stable nuclei are formed. Nucleation is then followed by a growth period, which ceases when monomer species are consumed. We show here (and below, in reference

to the work of others) that sigmoidal growth kinetics are also typically observed for aggregative nanocrystal growth (regime A in Figure 3).

However, sigmoidal growth kinetics are inconsistent with equilibrium Ostwald ripening. The conventional Lifshitz–Slyozov–Wagner (LSW) model for Ostwald ripening posits that the mean nanocrystal volume increases linearly in time (regime OR in Figure 3).[19,20] Moreover, Ostwald ripening is not a nucleation-driven process, and an initial induction period (like that in Figure 5) for the coarsening of nanocrystals having an initially broad size distribution is not expected.

Early time (nano)crystal-size distributions (CSDs) also provided strong evidence for aggregative growth in our studies of gold nanocrystal coarsening.[92] At times shortly after the end of the initial induction period, the CSDs were bimodal (Figure 6), with the smaller mode corresponding to the initial, primary
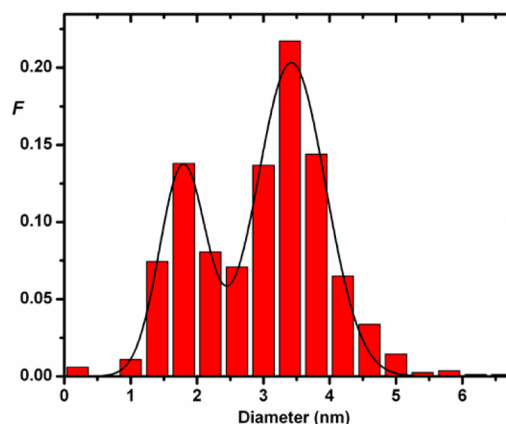

Figure 6. Diameter-distribution histogram of gold nanocrystals taken a few minutes after maximum nucleation rate (τ_n) was achieved. The crystal-size distribution (CSD) is strongly bimodal, with the smaller-size mode corresponding to primary nanocrystals, and the larger-size mode to the nanoparticles growing by aggregative processes. F is the fraction of nanocrystals of a specific diameter. Reprinted with permission from ref 92. Copyright 2010, American Chemical Society, Washington, DC.

nanocrystals, and the larger mode corresponding to critical-size aggregates of primary nanocrystals (aggregative nuclei; see below). Presumably, these critical-size aggregates corresponded to the stable-size aggregates identified by Bogush and Zukoski (see above).[55] As aggregates smaller than this size are unstable, a second peak emerges in the CSD, at the larger mode. Such bimodal size distributions are theoretically predicted for aggregative processes,[55,51,79,139−144] and have also been observed by other researchers.[44,145−153]

Significantly, under normal circumstances, Ostwald ripening is incapable of producing a bimodal size distribution, similar to those that we observed (Figure 6). Instead, Ostwald ripening produces a unimodal distribution that shifts and broadens during coarsening, but does not separate into two modes.[31,151,154−157] A bifurcation (into a bimodal distribution) by Ostwald ripening requires a coarsening-rate discontinuity at a critical nanocrystal size,[158] which is a special condition that is not present in our studies of gold nanocrystal growth. Experimental observations of bimodal CSDs are occasionally mistakenly attributed to Ostwald ripening.[92] Indeed, Ostwald ripening can *accentuate* a pre-existing bimodal distribution. However, except under very rare circumstances, Ostwald

ripening cannot *generate* a bimodal distribution. Thus, observation of early time bimodal CSDs should be attributed to aggregative growth rather than to Ostwald ripening.

Aggregative growth and Ostwald ripening may also be distinguished by nanoparticle core structure. Nanocrystals coarsened by Ostwald ripening should consist of a single crystalline domain, because they grow from single-crystalline primary nanocrystals by monomer addition. In contrast, nanoparticles grown by aggregation of primary nanocrystals should be initially polycrystalline. Over time, such polycrystalline nanoparticles may recrystallize to single crystals, develop multiply twinned structures as previously reported by Uyeda and co-workers[81] and Turkevich,[159] or remain polycrystalline.

High-resolution TEM imaging of gold nanoparticles harvested after 10 min under our coarsening conditions revealed 20%−40% of them to be polycrystalline.[92] These polycrystalline nanoparticles had mean crystalline-domain sizes of 1.5 nm, close to the diameter of the primary nanocrystals supporting their growth. After 60 min under coarsening conditions, ≥95% were single crystalline, and a minor fraction (≤5%) had become multiply twinned.

The results indicated that the initially polycrystalline secondary nanoparticles underwent recrystallization in time at the coarsening temperature (180 °C). For bulk phases, recrystallization temperatures are generally 33%−50% of the absolute melting point.[160] In our case, the gold nanoparticles recrystallized at 34% (453 K) of the absolute melting point of bulk gold (1337 K). Because gold nanocrystals melt at temperatures below the bulk melting point, the thermal conditions for recrystallization were clearly in place in our coarsening experiments. We surmised that all of the secondary nanoparticles were initially polycrystalline, as a result of aggregation and coalescence of the primary gold nanocrystals, prior to recrystallization. Our observation of polycrystalline secondary nanoparticles was inconsistent with Ostwald ripening.

4.2. Fitting Aggregative-Growth Kinetics: KJMA Approach.

We used a modified Kolmogorov−Johnson−Mehl−Avrami (KJMA) expression to fit the sigmoidal profile in Figure 5 (eq 1),

$$\frac{\bar{V}(t)}{\bar{V}_{\lim}} = \frac{\bar{V}_i}{\bar{V}_{\lim}} + \left(1 - \frac{\bar{V}_i}{\bar{V}_{\lim}}\right)\{1 - \exp[-(k_g t)^n]\} \quad (1)$$

where $\bar{V}_{\lim}$ is the nanocrystal mean volume at time t, $\bar{V}_{\lim}$ is the final nanocrystal mean volume, and $\bar{V}_i$ is the primary-nanocrystal mean volume. The KJMA model applies rigorously to specific types of solid-state phase transformation;[161−163] however, it has also been used to fit other nucleation-and-growth processes exhibiting sigmoidal conversion kinetics. These have included crystal or particle formation from both solution and melts.[91,164−170] The KJMA model has been previously applied to the solution-based nucleation and growth of nanocrystals.[171]

Equation 1 contains two fitting parameters: a rate parameter (k_g) and the Avrami exponent (n).[172] For solid-state phase transformations, the value of n is often related to the mechanism of nucleation and the dimensionality of growth.[161,173−175] Because of our nonrigorous application of the KJMA model to aggregative nanocrystal growth, we presume no physical interpretation of the fitted values of this exponent. In principle, the rate parameter k_g is derived from a convolution of nucleation and growth steps. In practice, we

have found it to be strongly correlated with aggregative-growth rates and insensitive to nucleation.[92] Similarly, k_g is fairly insensitive to the value of n.[92] Because of the lack of a fundamental physical definition of k_g in the application of the KJMA model to aggregative nanocrystal growth, we suggest that it is useful for comparing growth rates among closely similar growth processes. A modified KJMA model also distinguishes the onset time for Ostwald ripening (see below).

Other benefits to using the KJMA model as embodied in eq 1 and related equations (see below) for nanocrystal growth kinetics are its simplicity and the generally good fits it provides to the observed sigmoidal kinetic profiles. However, this application of the KJMA model also has detractions and detractors. Finke and Finney have pointed out that the lack of precise physical meaning to the parameters k (here, k_g) and n is a major drawback.[176] Moreover, k (here, k_g) is not a rate constant of the type encountered in standard chemical kinetics.[176] Skrdla has suggested that, although the KJMA model may be applied to classical, LaMer-like nanocrystal growth,[171] it is not well-used for aggregative processes.[77] Other kinetic models for aggregative nanocrystal growth have been presented, which are summarized below.

Oriented-Attachment Kinetics. Oriented attachment is a form of aggregative nanocrystal growth, the kinetics of which have been extensively investigated. Huang, Zhang, and Banfield studied the hydrothermal coarsening of ZnS nanocrystals in the presence of mercaptoethanol, finding that the kinetics corresponded to two distinct, consecutive growth regimes, the second (later) of which was consistent with Ostwald ripening.[60] The first growth regime was inconsistent with Ostwald ripening, and has been attributed to oriented attachment, for which the time dependence of the mean diameter (D) was described by eq 2, where D_0 is the mean diameter at $t = 0$ and k_1 is the rate constant for oriented attachment.

$$D = \frac{D_0(\sqrt[3]{2}\,k_1 t + 1)}{k_1 t + 1} \quad (2)$$

A subsequent study by these authors investigated the hydrothermal coarsening of ZnS nanocrystals in the absence of mercaptoethanol.[134] Under these conditions, the oriented-attachment and Ostwald-ripening regimes were found to significantly overlap, such that the kinetic data were best fit by eq 3:

$$D = \frac{D_0(\sqrt[3]{2}\,k_1 t + 1)}{k_1 t + 1} + k_2 t^{1/n} \quad (3)$$

where the first term described oriented attachment as in eq 2 and the second term described Ostwald ripening with k_2 being the rate constant and n being a constant. The results of these studies foreshadow the next subsection of this review, on the mechanistic regimes of nanocrystal growth.

Subsequently, Huang, Lin, and co-workers developed a multistep kinetic model for oriented attachment of ZnS nanocrystals based in the Smoluchowski equation.[135] This population-balance model accounts for the oriented attachment of nanoparticles of varying sizes, including those having already undergone prior oriented attachment, and requires numerical simulation to fit the kinetic data. This model was also applied to the multistep oriented attachment of PbS[64] and SnO₂[136] nanocrystals. In the latter case, the oriented attachment kinetics were not complicated by the occurrence of Ostwald ripening.

10

dx.doi.org/10.1021/cm402139r | *Chem. Mater.* 2014, 26, 5−21

Tsapatsis and co-workers elucidated an oriented-aggregation mechanism for the growth of zeolite (silicalite-1) crystals from silica sols.[133] The key observations supporting oriented aggregation were (1) the formation of 5-nm primary nanoparticles followed by an induction period prior to the emergence of a second population of much larger silicalite-1 particles, (2) the aggregate-like morphologies of the initially formed silicalite-1 particles having crystalline domain sizes equal to those of the primary nanoparticles, and (3) the successful fit of a quantitative aggregation model to the experimental kinetic data. We note that these observations are important indicators of aggregative-nanoparticle growth (see subsection 4.1). The mechanistic model employed a rate constant for coalescence (β) calculated from Derjaguin–Landau–Verwey–Overbeek (DLVO) theory.[177−179] Simulations using β and a multistep aggregation process were shown to fit the size vs yield and yield vs time data. These results were expanded in a follow-up publication.[52]

In 2004, Penn suggested that oriented attachment could be analyzed with conventional chemical kinetics by considering the primary nanoparticle (P) to be a molecular reactant.[56] She demonstrated that the growth kinetics were consistent with the mechanism in eq 4, in which the primary nanoparticles are in equilibrium with an outer-sphere dimer complex (P···P), such that the primary nanoparticles are able to rotate and reorient relative to each other. When an appropriate mutual orientation is achieved, attachment occurs yielding the coalesced particle P–P. The rate law for this mechanism (eq 5) is second order in primary-nanoparticle concentration. Penn noted that rate data previously reported by Huang, Zhang, and Banfield[60] for oriented aggregation of ZnS nanocrystals was indeed second order in primary nanoparticles.

$$P + P \underset{k_{-1}}{\overset{k_1}{\rightleftharpoons}} P\cdots P \overset{k_2}{\rightarrow} P-P \tag{4}$$

$$\frac{d[P-P]}{dt} = \left(\frac{k_1}{k_{-1}}\right) k_2 [P]^2 \tag{5}$$

Penn and co-workers subsequently applied the same mechanism (eq 4) and rate law (eq 5) to the growth of goethite nanorods from primary ferrihydrite nanoparticles.[180] Plots of inverse primary-nanoparticle concentration ($[P]^{-1}$) versus time were linear, as expected for second-order kinetics. The authors compared the measured rate constants with the DLVO-theory-derived β rates calculated according to Tsapatsis and co-workers,[133] finding the experimental values to be many orders of magnitude smaller. The experimental rate constants were also shown to increase with decreasing primary-nanoparticle size.

Penn and co-workers subsequently studied the effects of ionic strength and primary-nanoparticle size on oriented-aggregation rates in more detail.[181] As above, the experimental plots of $[P]^{-1}$ versus time were linear, in accord with second-order kinetics, at various ionic strengths and primary-nanoparticle sizes. The oriented-aggregation rate constant (k) was found to increase with increasing ionic strength and decreasing primary-nanoparticle size. The increase in k with increasing ionic strength followed the expected trend, but the experimental values were again many orders smaller than the DLVO-theory-derived β rates.

Pseudo-elementary-Step Kinetics. In 1997, Finke and Watzky introduced a new two-step kinetic model for nanocrystal formation.[43] In its initial form, this model accounted for the classical regime of nucleation and growth, but did not address aggregation. Experimentally, the growth kinetics were followed by a reporter reaction catalyzed by the growing nanoparticles, in which the nanoparticle growth was monitored by the kinetics of nanocrystal-catalyzed cyclohexene reduction to cyclohexane. The proposed mechanism included slow, continuous nucleation (steps of type 1, eq 6) and fast, autocatalytic surface growth (steps of type 2, eq 7), where A represents the metal-containing nanoparticle precursor, and B catalytic sites on the growing iridium nanoparticles.

$$A \overset{k_1}{\rightarrow} B \tag{6}$$

$$A + B \overset{k_2}{\rightarrow} 2B \tag{7}$$

Equations 6 and 7 constitute pseudo-elementary steps, each of which occurs many times, as determined by the relative values of k_1 and k_2, until all of precursor A is consumed. The sigmoidal kinetics of the reporter hydrogenation reaction were fit by the integrated rate law in eq 8, affording the experimental rate constants k_1 and k_2.

$$[A]_t = \frac{\frac{k_1}{k_2} + [A]_0}{1 + \frac{k_1}{k_2[A]_0} \exp[(k_1 + k_2[A]_0)t]} \tag{8}$$

At that time, the authors claimed the mechanism represented by eqs 6 and 7 to be the first new mechanism for transition-metal nanoparticle formation in 45 years.[43]

In subsequent studies, Finke and co-workers encountered experimental kinetic profiles that could not be fit by the two-step mechanism.[45−47,49,50] These cases required the addition of one (eq 9) or two (eqs 9 and 10) aggregation (agglomeration) steps to fit the experimental data, where C represents a nanocrystal aggregate (agglomerate). As mentioned above, eqs 9 and 10 constitute pseudo-elementary steps, each of which is repeated in accordance with the values of the rate constants k_3 and k_4. Equation 9 was defined as a bimolecular-agglomeration step, and eq 10 as an autocatalytic agglomeration step. The integrated rate law for the four-step mechanism (eqs 6, 7, 9, and 10) could not be expressed in analytical form, and extraction of the rate constants k_1-k_4 required curvefitting by numerical methods. We note that the proposed bimolecular-agglomeration step (eq 9) resembles a nonclassical, aggregative-nucleation step (see below), and the proposed autocatalytic-agglomeration step (eq 10) resembles stepwise aggregative growth by sequential addition of primary nanocrystals.

$$2B \overset{k_3}{\rightarrow} C \tag{9}$$

$$B + C \overset{k_4}{\rightarrow} 1.5C \tag{10}$$
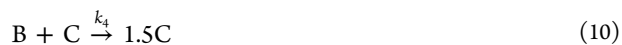
Finke and Finney also studied the relationship between the KJMA model and the two-step Finke–Watzky (FW) model, and their relative abilities to fit sigmoidal kinetic data.[176] Several sets of experimental kinetic data for solid-state phase transformations were taken from the literature and fit by both the KJMA and FW models. In two-thirds of these cases, the data were fit equally well by the two models. In addition, Finney and Finke derived the functional relationships of the KJMA k_g and n (eq 1) to the FW k_1 and $k_2[A]_0$ (eqs 6 and 7), showing k_g and n to be convolutions of k_1 and $k_2[A]_0$. Finally, Finke and co-workers successfully refit the aggregative-growth kinetics of Buhro and co-workers[63] (such as in Figure 5) using

11

dx.doi.org/10.1021/cm402139r | *Chem. Mater.* 2014, 26, 5−21

the FW model for the aggregative steps in eqs 9 and 10. We find it compelling that the FW model, which has been designed for classical nucleation and growth processes, is applicable to aggregative processes, for which we propose nucleation and growth components (see below).

Dispersive Kinetic Models. We note, in passing, that Skrdla and Robertson have proposed dispersive kinetic models that address the classical nucleation and growth of nanocrystals.[77,78,171,182,183] Such models recognize that growth rates must vary with the size of the growing nanocrystal, requiring that a dispersion of activation energies (rate constants) must exist. The rate laws are expressed in analytical form, such as eq 11,

$$x = \exp\{\alpha t[\exp(-\beta t^2) - 1]\} \qquad (11)$$

where x is the remaining monomer at time t, and α and β are empirical (fitting) parameters related to a t-independent activation enthalpy and t-dependent activation entropy, respectively.[78] However, Skrdla did not apply the dispersive kinetic approach to aggregative growth, because he does not consider it a conversion mechanism (phase transformation). Instead, he invoked the traditional DLCA and RLCA mechanisms to describe aggregation.[77]

4.3. Mechanistic Regimes of Nanocrystal Growth. Three modes of nanocrystal growth have been discussed here: classical (LaMer) nucleation and growth, aggregative growth, and Ostwald ripening (see Figure 3). In this subsection, we show that all three modes may contribute to a given nanocrystal-growth process, in successive temporal regimes and in the sequence given in Figure 3. Or, these growth regimes may have varying degrees of temporal overlap. As noted above, oriented attachment and Ostwald ripening may occur in successive or overlapping regimes. Results summarized here indicate that classical LaMer and aggregative growth may also occur successively or with overlap. Conditions under which the three growth modes are temporally well-separated provide an experimental window for mechanistic characterization of aggregative growth.

In seminal, early work, Van Hyning, Klemperer, and Zukoski studied the formation of silver nanoparticles by the aqueous borohydride reduction of Ag^+ ions.[57,184] Early time monitoring determined that the concentration of Ag^+ was diminished by two orders of magnitude within a few seconds of reagent mixing, establishing an effectively complete reduction of Ag^+ to Ag^0 on that time scale. Within the same early time period, a distribution of small, primary silver nanocrystals having dimensions of 2−3 nm was produced.

These primary nanocrystals grew to 10−20 nm over the subsequent 20−60 min. Since the concentration of Ag^+ nutrient was vanishingly small during this subsequent period, the continued growth could not be ascribed to the reduction of Ag^+ to Ag^0 at the nanoparticle surfaces. Thus, classical LaMer nucleation and growth was confined to the first few seconds, and the subsequent growth must therefore have occurred via a different process.

The authors observed that the final silver nanoparticle mean size and dispersity were insensitive to the initial primary particle size and size distribution, and thus to the initial stages of the reaction, including reagent mixing. This observation indicated that the initial classical LaMer nucleation and growth did not significantly influence the final mean size and dispersity. Instead, the final nanoparticle sizes and growth rates were highly dependent on temperature, borohydride concentration, and ionic strength, which determined nanoparticle surface

potentials. The results pointed to the aggregation and coalescence of nanoparticles as the principle growth mechanism, as nanoparticle pair-interaction potentials are governed by the interplay of van der Waals attraction and electrostatic repulsion.

Consequently, the authors developed a quantitative aggregative-growth model using a population-balance approach based on Smoluchowski theory. Pair-interaction potentials were estimated by the DLVO approximation. The model semi-quantitatively predicted the time evolution of particle size as functions of temperature and ionic strength, with the quantitative discrepancies ascribed to small differences between measured and calculated surface potentials. The ability of the model to predict final nanoparticle-size increases in response to ionic-strength increases affirmed the form of the pair-interaction potential, based only on van der Waals attractions and electrostatic repulsions. Moreover, the results demonstrated aggregation and coalescence capable of achieving narrow dispersities, and control of growth rates and final mean nanoparticle sizes through conditions that influence pairwise aggregation.

Emmerling, Kraehnert, Polte and co-workers reported important studies elucidating temporal regimes (or phases) of metallic nanoparticle growth.[61,62,185] These studies were conducted with in situ monitoring by X-ray absorption near-edge structure (XANES) and small-angle X-ray scattering (SAXS), which allowed real-time determination of nanoparticle mean size and number density (SAXS), and mean metal oxidation state (XANES).

An initial investigation[185] pursued the mechanism of gold nanoparticle growth by citrate reduction of Au^{3+} (by the well-known Turkevich method[186]). Approximately 20% of the Au^{3+} was reduced to polydisperse primary gold nanoparticles with a mean diameter of 4 nm within the first 60 s, which underwent aggregation and coalescence to 8-nm mean-diameter nanoparticles over 20 min (Figure 7). In the following growth phase,
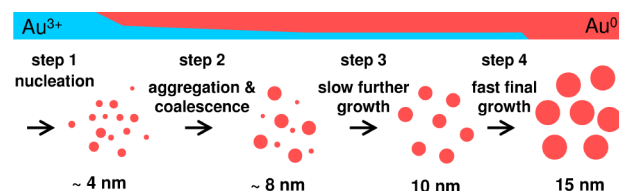

Figure 7. Schematic illustration for the process of gold nanocrystal formation by citrate reduction of Au^{3+} (the Turkevich method[186]). Adapted with permission from ref 185. Copyright 2010, American Chemical Society, Washington, DC.

the nanoparticles grew slowly to a mean diameter of 10 nm over the next 30 min by surface reduction of Au^{3+} and classical growth. In the final growth phase, the mean diameters of the nanoparticles grew rapidly to 15 nm via autocatalytic surface reduction as the remaining Au^{3+} was consumed. The polydispersity continuously narrowed over the entire time scale of the process. The results established that aggregation, not classical nucleation, determined the number of growing gold nanoparticles, and was involved in producing the final low polydispersity. Moreover, the study demonstrated that aggregation and coalescence may overlap temporally with classical growth.

In a subsequent study, the authors examined the growth mechanism for the reduction of Au^{3+} by the stronger reducing

agent borohydride, which is a much faster reaction.[61] Monitoring found that all Au^{3+} was reduced to metallic gold, in the form of primary nanoparticles with a mean diameter of 1.6 nm, within the first 200 ms. Subsequently, the nanoparticles grew by aggregation and coalescence, with a concomitant decrease in number density, to 3.4 nm. Thus, with the stronger reducing agent, classical nucleation and growth, and aggregation and coalescence were separated into separate, successive time regimes.

The authors then elucidated the silver-nanoparticle growth mechanism upon the reduction of Ag^+ by borohydride.[62] The mechanism was found to be closely related to that for the borohydride reduction of Au^{3+},[61] with one important difference. Silver nanoparticles grew principally by aggregation and coalescence; however, two distinct periods of aggregation and coalescence were observed. As was previously established by Van Hyning, Klemperer, and Zukoski,[57] complete reduction of Ag^+ to Ag^0 was assumed within the first milliseconds of reaction, yielding, in this case, 2-nm-diameter primary nanoparticles. These grew by aggregation and coalescence, with decreasing nanoparticle number densities, to 4.6-nm-diameter nanoparticles within the following 2 s.

Nanoparticle growth subsequently paused for 6−8 min, in an intermediate period of size stability. After this intermediate pause, growth resumed in a second stage of aggregation and coalescence to afford 12-nm-diameter silver nanoparticles. The intermediate period of stability was attributed to surface stabilization by borohydride coordination. The borohydride hydrolyzed over 6−8 min, ultimately initiating the second stage of growth, as previously suggested by Van Hyning and Zukoski.[184] As in the borohydride reduction of Au^{3+} (see above), classical LaMer growth and aggregative growth occurred in consecutive, nonoverlapping periods. The authors concluded that aggregation and coalescence is the dominant growth mechanism in cases when the monomer-supplying chemical reaction is faster than the overall growth process.

A related SAXS study of silver-nanoparticle growth by citrate reduction of Ag^+ was conducted by Takesue and co-workers.[187] Under the conditions investigated, growth was accomplished within 10 ms. An initial induction period (0−0.39 ms) in which reduction of Ag^+ occurred was followed by a nucleation period (0.59−0.79 ms) in which Ag_{13} nanoclusters 0.7 nm in diameter were formed. Subsequently, growth occurred by aggregation of the Ag_{13} nanoclusters. Again, classical LaMer and aggregative growth were observed to occur in consecutive regimes.

We also elucidated a mechanism of silver nanoparticle growth, by reaction of bis(triphenylphosphine)silver(I) myristate $[(PPh_3)_2Ag(O_2CC_{13}H_{27})]$ and azoisobutyronitrile (AIBN) in the presence of a PHD-co-PVP polymer stabilizer and in a nonaqueous dispersion (see eq 12).[94] The rate of Ag-

$$\text{(12)}$$
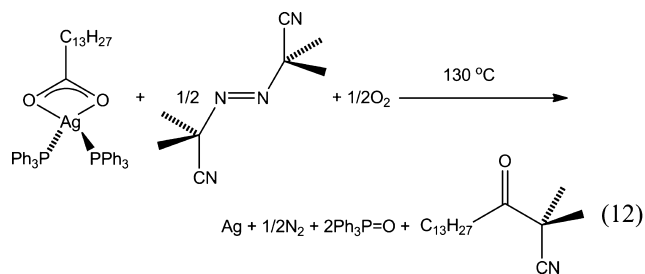
precursor conversion was monitored by ^{31}P NMR, using the disappearance of the precursor PPh_3 and the appearance of the

product $Ph_3P=O$ resonances. The conversion kinetics were first order in precursor concentration, with a half-life of $t_{1/2} = 3.65 \pm 0.42$ min, establishing the time scale for classical LaMer nucleation and growth.

Silver-nanoparticle growth was monitored over 70−100 min. Primary nanocrystals 1.8 ± 0.6 nm in diameter were observed to form within the initial 3−4 min, after which a bimodal size distribution containing the primary nanocrystals and distinctly larger silver nanoparticles formed. The primary nanocrystals were consumed over 50−60 min as the larger nanoparticles continued to grow, achieving diameters of 7.3 ± 0.7 nm in this period. High-resolution transmission electron microscopy (HRTEM) analyses established the vast majority of these larger nanoparticles to be polycrystalline. The bimodal distributions and polycrystallinity provided strong evidence for aggregative growth (see subsection 4.1 above).

The silver-nanoparticle growth kinetics are plotted in Figure 8, as the mean nanoparticle volume $(\bar{V}(t))$ versus time.
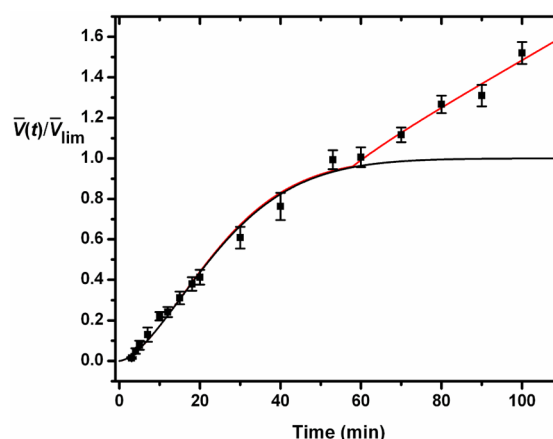

Figure 8. Kinetic data and the eq 13 fit (red curve) for silver-nanocrystal growth. The black curve plots only the first term from the eq 13 fit. $\bar{V}_{lim}$ is the mean volume at the end of active growth (at 60 min). Reprinted with permission from ref 94. Copyright 2010, American Chemical Society, Washington, DC.

Classical LaMer nucleation and growth could account for only the first 10−15 min of growth (3−4 half-lives of precursor disappearance). This period was consistent with the initial burst of primary nanocrystal formation, but not for the sustained growth that occurred thereafter. The data in the range of 15−100 min were nonlinear and, therefore, inconsistent with Ostwald ripening over the entirety of that range. As detailed above, aggregative nucleation and growth exhibits a sigmoidal profile that can be fit by a KJMA expression. However, only the data up to ∼60 min could be fit in this manner (see the black curve in Figure 8). Therefore, we surmised that the growth after ∼60 min was due to Ostwald ripening.

Consequently, we fit the Figure 8 kinetic data with eq 13 (red curve), which contains a first term (a KJMA term) for aggregative growth, and a second term for Ostwald ripening. In the second term, the Ostwald-ripening rate parameter k_{OR} is multiplied by a logistic turn-on function to activate Ostwald ripening at time τ_{OR}. The parameter ω determines the time width of the turn-on period and was arbitrarily set.

$$\frac{\overline{V}(t)}{\overline{V}_{\text{lim}}} = \{1 - \exp[-(k_g t)^n]\}$$

$$+ \left\{ \frac{t - \tau_{OR}}{1 + \exp[-2\omega(t - \tau_{OR})]} \right\} k_{OR} \qquad (13)$$

We note that the later, Ostwald-ripening regime (Figure 8) provides a linear growth in silver-nanoparticle mean volume in accord with LSW theory.[19,20] The fitted value of τ_{OR} was 57.9 ± 3.4 min, indicating the secession of aggregative growth and the onset of Ostwald ripening at that time. A second quantitative measure of the onset time for Ostwald ripening was the minimum in the width of the nanoparticle diameter distribution, which occurred at 60 ± 5 min, in excellent agreement with τ_{OR}.

The results established that classical LaMer nucleation and growth occurred from 0 to 15 min, aggregative growth occurred from 5 min to 60 min, and Ostwald ripening occurred from 60 min to 100 min. Thus, the three nanoparticle growth modes each contributed to the silver-nanoparticle size evolution, but in successive time regimes with little overlap. The work described earlier in this subsection demonstrated that classical LaMer growth and aggregative growth occur in sequential or partially overlapping regimes. The work on oriented attachment (see subsection 4.2) demonstrated that aggregative growth and Ostwald ripening occur in sequential or partially overlapping regimes. The presently discussed study demonstrated that all three growth modes may occur in consecutive regimes, and exhibited the sequence in which the growth modes normally occur, as depicted in Figure 3.

Similarly, we studied the mechanism of bismuth-nanoparticle growth, by thermal decomposition of $Bi[N(SiMe_3)_2]_3$ in the presence of a PHD-co-PVP polymer stabilizer at 180 °C.[95] Primary nanocrystals having diameters of 1.9 ± 0.4 nm were observed to form within the initial 2 min, after which a bimodal size distribution formed, containing the primary nanocrystals and distinctly larger bismuth nanoparticles. The primary nanocrystals were consumed over 75−120 min as the larger nanoparticles continued to grow, achieving 20−30 nm diameters in this period. After 75−120 min, size-distribution broadening was observed, consistent with Ostwald ripening. The early time bimodal distributions evidenced aggregative growth prior to Ostwald ripening.

A representative set of bismuth nanoparticle growth-kinetics data is given in Figure 9. These data were also well fit by eq 13, yielding the curve shown. The sigmoidal portion of the curve is due to aggregative growth, and the later linear portion to Ostwald ripening. For synthetic purposes, the Ostwald ripening in Figures 8 and 9 would be prevented, such that the syntheses would reliably produce narrow diameter distributions and final mean sizes determined by the aggregative-growth process. Indeed, we were able to identify such conditions for the growth of bismuth nanoparticles.[188] The success of eq 13 in fitting the silver- and bismuth-nanoparticle growth data suggest that it might be more generally applied to determining the end of aggregative growth and the onset of Ostwald ripening in other nanoparticle systems.

As noted above, the three common growth modes may overlap temporally. A study of platinum-nanoparticle growth by a photoreduction process by Harada and Kamigaito found the classical LaMer and aggregative growth regimes to overlap.[66] A related study of silver-nanoparticle growth by Harada and co-workers seemingly found all three growth modes to overlap to
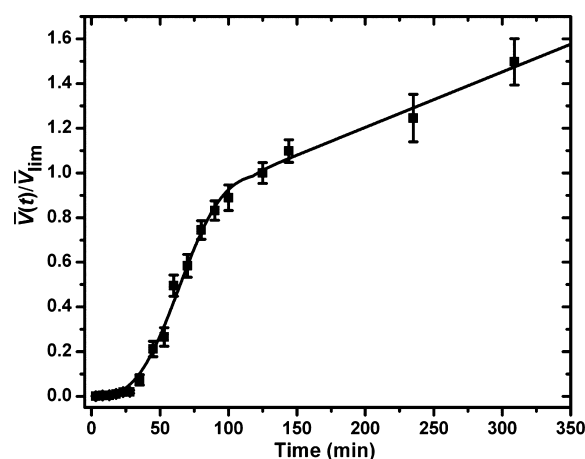

Figure 9. Kinetic data and the eq 13 fit for bismuth-nanocrystal growth. Reprinted with permission from ref 95. Copyright 2011, American Chemical Society, Washington, DC.

varying extents, with aggregative growth making a small overall contribution.[189] Another study of rhodium- and palladium-nanoparticle growth by Harada and co-workers failed to identify an aggregative-growth component.[190]

4.4. Nonclassical Nucleation in Aggregative Processes. We have argued that the initial stages of aggregative growth may be considered a nonclassical nucleation process.[55,76,116,191−195] We and others have shown that (i) the initiation of aggregative growth can determine the number of growing nanoparticles or nanocrystals, and (ii) aggregative growth is capable of producing narrow final nanoparticle-size distributions from primary nanoparticles having comparatively broad dispersities,[53,54,57,92,94,95,184,196−198] suggesting that the initiation is a nucleation-like event. Aggregative growth also has induction periods and other characteristics that mimic classical nucleation (see Figure 3).[31,45−47,49,50,60,92,94,95,171,199] This subsection will show that the induction of aggregative growth may either be a nonclassical nucleation, or modeled as one, although the underlying physics is different from that in classical nucleation.

As is well-known from classical nucleation theory, the thermodynamic driving force for crystal growth is the lattice energy or cohesive energy released by assembly of the crystal lattice. The nucleation barrier to be overcome at small crystal-nucleus sizes is generated by the interfacial energy between the crystal-nucleus surface and the phase it is growing within. Because the released lattice (cohesive) energy grows as the cube of the radius, and the consumed interfacial energy only as the square of the radius, growth ultimately becomes spontaneous for crystal-nuclei surpassing a critical size. The lattice and interfacial energies are precisely offsetting at the critical size, indicating that a critical-sized nucleus has an equal probability of growing or redissolving into the growth phase. Classical nucleation is the process of generating critical-sized nuclei through the interplay of lattice (cohesive) and interfacial energies.

For small, primary nanoparticles, substantial lattice or cohesive energy has already been released, and substantial interfacial (surface) energy already paid for, prior to the onset of aggregative growth. And yet, activation-energy barriers to aggregative growth do exist, for both DLCA and RLCA processes,[77] which are necessarily generated by different physical interactions than those involved in classical nucleation.

These interactions were identified above in conjunction with the DLVO model, and its use to fit the aggregative-growth kinetics of silver nanocrystals (subsection 4.3).[57,184] The attractive interactions that promote aggregation are van der Waals forces, and the inhibiting interactions are electrostatic or other interparticle repulsions. One imagines constructing a critical-size aggregate (a nonclassical nucleus) by assembling a sufficient number of primary particles such that the van der Waals attractions and electrostatic repulsions are precisely offsetting.

Indeed, the colloidal crystallization of polymer or silica spheres, which is inherently an aggregative process, has long been used to model classical nucleation and growth. Such studies[91,96,100] have allowed the determination of critical-nucleus (aggregate) sizes, and entire nucleation functions (see section 2), although the underlying physics are quite different from those of classical nucleation.

Recent studies have found that prenucleation clustering of growth monomers contributes to crystallization processes involving biomineralization, proteins, and colloids.[194,195] For $CaCO_3$ crystallization, the average prenucleation cluster diameters were found to be ~2 nm, or roughly 70 ions in size.[195] Evidence was obtained showing that nucleation proceeded by cluster–cluster aggregation, rather than by individual cluster growth. The nucleation barriers were hypothesized to be due to structural rearrangements within the prenucleation clusters in this nonclassical nucleation process.[195] Similarly, so-called magic-size nanoclusters, such as $(CdSe)_{13}$, $(CdSe)_{19}$, $(CdSe)_{33}$, and $(CdSe)_{34}$[200] have long been observed as intermediates preceding the nucleation of colloidal semiconductor nanocrystals.[201–204] The tantalizing suggestion is that perhaps many nucleation processes that were formerly considered to occur by the classical process are actually aggregative.

Finally, we demonstrate in the following section that meaningful nucleation functions (such as in Figure 2) may be extracted from experimental kinetic data for aggregative nanocrystal growth. We will show that the final mean nanoparticle sizes and size distributions correlate strongly with the experimental parameters extracted from these nucleation functions (see section 2). If the initial stages of aggregative growth could not be modeled as a nucleation process, then we could not have determined these nucleation functions, and they would have no correlation with the outcome of experimental aggregative-growth processes. The fact that they do correlate provides strong justification for modeling the initiation of aggregative growth as a nucleation event.

5. THE EXPERIMENTAL NUCLEATION FUNCTION

As discussed above (see section 2), the time dependence of the nucleation rate, $\Gamma(t)$, is the nucleation function. Prior to nucleation, the nucleation rate is zero. During nucleation, $\Gamma(t)$ rises, then falls, and returns to zero at the conclusion of the nucleation period. Ideally, and typically, nucleation is confined to a narrow, early time window in the overall nanoparticle growth process.

An example of an experimentally determined nucleation function is given in Figure 10.[92] The more extensively determined nucleation functions of Wette and co-workers are slightly asymmetric and may have somewhat flattened tops.[91,96] However, our nucleation-rate data are fit well by Gaussian functions, and, thus, each nucleation function is defined by only
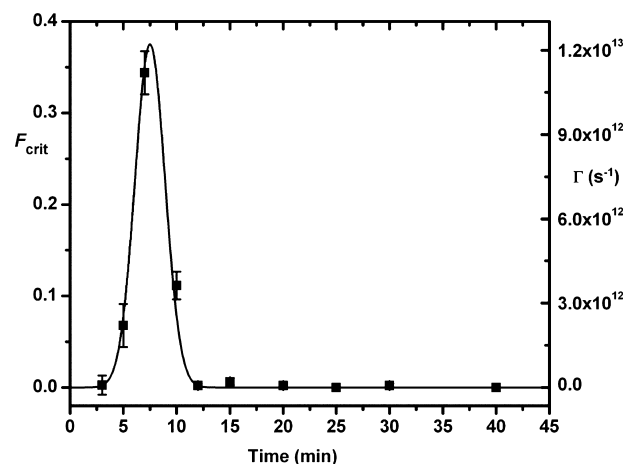

Figure 10. The aggregative-nucleation function (Gaussian fit) for silver-nanocrystal growth. The left and right axes correspond to the critical-aggregate fraction (F_{crit}) and the scaled nucleation rate ($\Gamma(t)$), respectively. Reprinted with permission from ref 94. Copyright 2010, American Chemical Society, Washington, DC.

three parameters: Γ_{max} (height), Δt_n (2σ width), and τ_n (peak-center time).

We argue here, and in section 2, that control of the nucleation function, or nucleation control, is the key to achieving purposeful control of final mean nanocrystal sizes and size distributions. Nucleation control requires that the nucleation parameters, and particularly the maximum nucleation rate Γ_{max} and the nucleation time width Δt_n, be measurable, and purposefully variable. The following subsections describe how the nucleation functions are extracted from experimental data, and how the nucleation parameters are manipulated.

5.1. Experimental Determination of the Nucleation Function. Wette and co-workers constructed nucleation functions for the colloidal crystallization of charged polymer spheres from image analyses of frames captured by video microscopy.[91] They directly counted the numbers of crystallites that appeared in fixed, successive time intervals throughout the nucleation period.

We determined nucleation functions for gold, silver, and bismuth nanocrystal growth by analysis of early time (nano)-crystal-size distributions (CSDs) measured by TEM. At the earliest times, the nanoparticle populations consisted only of the primary nanocrystals, which are at the small-size detectable limit for TEM measurement. Consequently, the corresponding CSDs had an asymptotic shape, which tailed off to larger nanocrystal size (or volume; see the black curve in Figure 11a).

After an induction period, aggregative nucleation was accompanied by the emergence of a peak in the CSD at the critical-aggregate (aggregative nucleus) size (or volume; see the red and green curves in Figure 11a),[55,79,140–143] which generated a bimodal distribution consisting of remaining primary nanocrystals and critical-sized aggregates. The emergence of the critical-aggregate peak was due to a burst of aggregative nucleation and a rapidly rising nucleation rate $\Gamma(t)$ (as in Figure 10),[79,139] and the survival of aggregates only at or larger than this critical size. Subsequently, the peak for the larger mode shifted to larger volume, as aggregative growth occurred upon the critical aggregates and $\Gamma(t)$ decreased from its maximum, Γ_{max} (see Figure 11b). Concurrently, the smaller
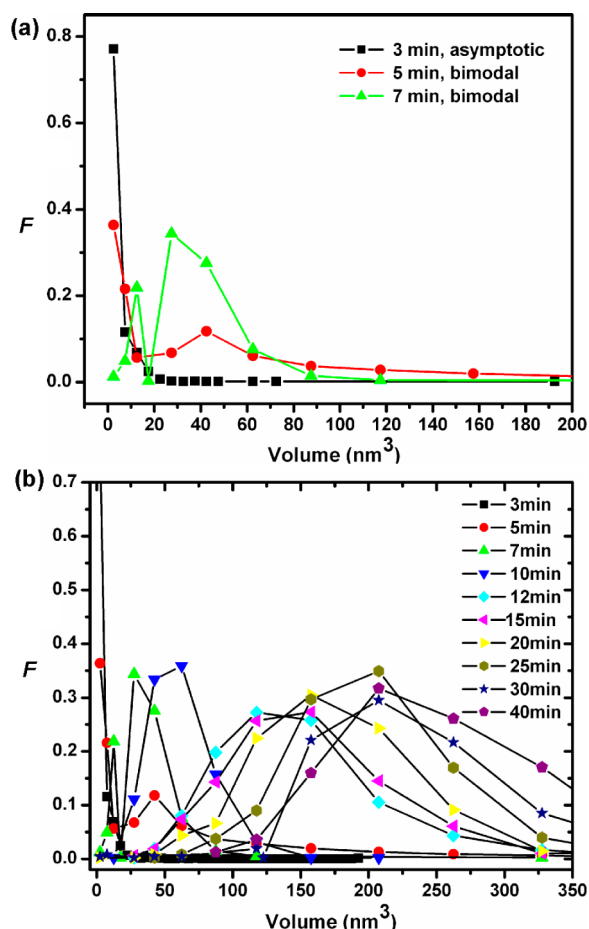
(a)

(b)

Figure 11. An extensive series of (nano)crystal-size distributions (CSDs) determined at various times (inset) in a silver-nanocrystal growth trial. The plots in (a) are an enlarged portion from (b) in the small nanocrystal volume regime, showing only the evolution of the CSDs from asymptotic to bimodal in the first 7 min of reaction. The fraction F of nanocrystals in a given volume bin is plotted against nanocrystal volume. Reprinted with permission from ref 94. Copyright 2010, American Chemical Society, Washington, DC.

mode shrank as the primary nanocrystals were consumed by aggregative growth.

Thus, the fraction (F_{crit}) of the nanoparticles (aggregates) within the CSD having the critical size (volume) rises and falls with the rise and fall of $\Gamma(t)$. We have proposed that this critical-size fraction F_{crit} is proportional to $\Gamma(t)$.[92] Therefore, a plot of $F_{crit}(t)$ vs t is proportional to the nucleation function, $\Gamma(t)$ vs t. Experimental $F_{crit}(t)$ vs t data are plotted in Figure 10, and fit by a Gaussian function.

The $F_{crit}(t)$ function must be rescaled to provide the nucleation function. Rescaling is accomplished by determination of N, the number of growing aggregates (aggregative nuclei), which is calculated from the stoichiometric amount of the final phase (in these cases, silver, gold, or bismuth) and the final mean nanoparticle size. Because the area under the nucleation function is N, the height of the nucleation function Γ_{max} is calculated using eq 14.[92] The remaining $F_{crit}(t)$ points are linearly scaled as $\Gamma(t)$ values using the $\Gamma_{max}/(\max F_{crit})$ ratio. The entire nucleation function is then described by eq 15, where Δt_n and τ_n are fitting parameters.

$$\Gamma_{max} = \frac{N}{\Delta t_n \sqrt{\frac{\pi}{2}}} \tag{14}$$

$$\Gamma(t) = \frac{N}{\Delta t_n \sqrt{\frac{\pi}{2}}} \exp\left[-\frac{2(t - \tau_n)^2}{\Delta t_n^2}\right] \tag{15}$$

In the following subsection, nucleation functions determined in this manner under a range of conditions are analyzed to determine how the nucleation parameters Γ_{max} and Δt_n may be purposefully varied. To achieve ideal nucleation control over final sizes and size distributions, Δt_n must be minimized, and Γ_{max} purposefully controlled over a wide range (see section 2).

5.2. Experimental Manipulation of the Nucleation Function. The important, early study by Bogush and Zukoski discussed above (see section 4) established that aggregative nucleation and growth is due to the colloidal instability, with respect to aggregation, of small primary nanoparticles.[55] Colloidal dispersions are generally stabilized against aggregation by steric or electrostatic repulsions, or their combination. Consequently, any condition that influences steric or electrostatic interactions between primary nanoparticles may, in principle, influence aggregative nucleation. These include the following factors: ionic strength (varied with salt additives);[57] the presence of polymer stabilizers, ligands, or surfactants; the primary nanoparticle number density (in the dispersion) or precursor concentration; temperature; and solvent. These conditions may be varied to determine their effects on the nucleation function.

In one such study, we determined the nucleation functions (according to subsection 5.1) for the aggregative growth of decanethiolate-capped gold nanocrystals at various concentrations of the salt additive tetra-n-octylammonium bromide (TOABr).[92,137,138] The results are shown in Figure 12. With
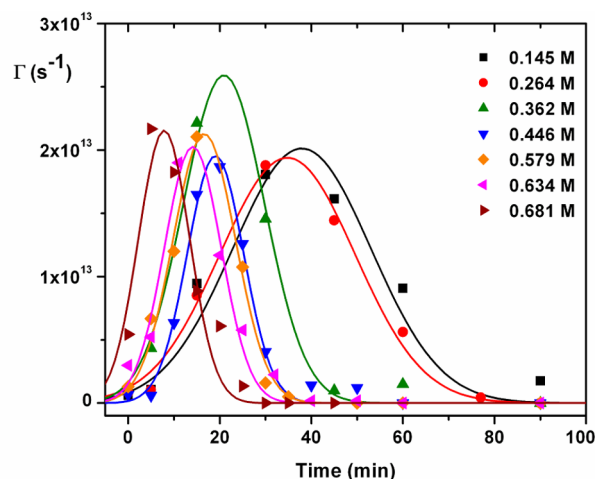

Figure 12. Nucleation functions for aggregative growth of gold nanocrystals conducted at various tetra-n-octylammonium bromide (TOABr) concentrations. Reprinted with permission from ref 92. Copyright 2010, American Chemical Society, Washington, DC.

increasing TOABr concentration, Δt_n progressively decreased to a minimized value. The nucleation parameter τ_n (peak-center time) also decreased, indicating increasing nucleation rates with increasing TOABr concentration. Interestingly, the maximum nucleation rate Γ_{max} (peak height) was fairly constant, with all values within experimental error of each other. Thus, the salt

additive accelerated nucleation and shrank the time window for nucleation, without significantly influencing Γ_{max}.

The results were interpreted using an electrical double-layer model. The decanethiolate-capped gold nanocrystals were synthesized using TOABr as a phase-transfer agent,[205] and retained residual TOABr in isolated form.[206] Consequently, the primary gold nanocrystals were both sterically and electrostatically stabilized (see Figure 13). The electrostatic stabilization
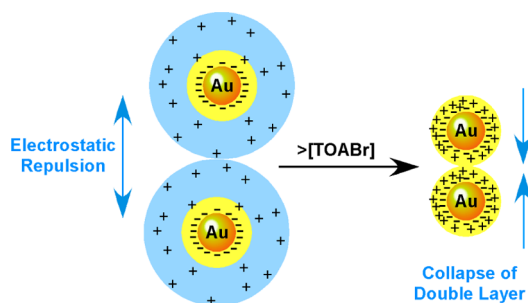

Figure 13. Schematic depiction of the collapse of the electrical double layer about the gold nanocrystals with a sufficient amount of added TOABr. The yellow region surrounding the gold nanocrystal core represents the thiolate monolayer, and the light-blue region represents the double-layer (the extent of the octyl$_4$N$^+$counterion atmosphere). The octyl$_4$N$^+$ ions are depicted by plus signs, and the Br$^-$ ions attached to the gold surfaces are depicted by minus signs. Reprinted with permission from ref 92. Copyright 2010, American Chemical Society, Washington, DC.

resulted from repulsive interactions between the n-octyl$_4$N$^+$ counterion atmosphere surrounding each primary nanocrystal (the double layer). The increased ionic strength of the medium induced by the added TOABr screened the mutual repulsions between n-octyl$_4$N$^+$ ions, shrinking the counterion atmospheres, and removing or minimizing the electrostatic stabilization. Therefore, aggregative-nucleation rates increased with increasing TOABr concentration.

The nucleation functions in Figure 12 enabled clear predictions about the final mean nanoparticle sizes and size distributions. Because Δt_n narrowed with increasing TOABr concentration, so too should the dispersity of the final diameter distribution. That is, the width of the nucleation function and the width of the final size distribution should follow each other. Figure 14a shows that indeed they did, except at the two highest TOABr concentrations, where size control was lost due to the very high viscosities of the growth dispersions.

The nucleation functions depicted in Figure 12 also enabled predictions about the final mean nanoparticle sizes. The final mean size should anticorrelate with N, the number of growing nanoparticles, given that the same amount of gold was used in each trial. The parameter N is the area under the nucleation function, which is the (scaled) product of Δt_n and Γ_{max}. However, the parameter Γ_{max} remained effectively constant in Figure 12, indicating that N should be determined predominantly by Δt_n. Thus, the final mean size and Δt_n were expected to anticorrelate, as shown by Figure 14b. The important conclusion is that the nucleation parameters derived from the nucleation functions determined the final nanoparticle mean size and size distribution resulting from aggregative growth.

In a related study, we determined the nucleation functions for the aggregative growth of bismuth nanocrystals from the precursor Bi[N(SiMe$_3$)$_2$]$_3$ in the presence of various concentrations of the salt additive Na[N(SiMe$_3$)$_2$].[95] These nucleation
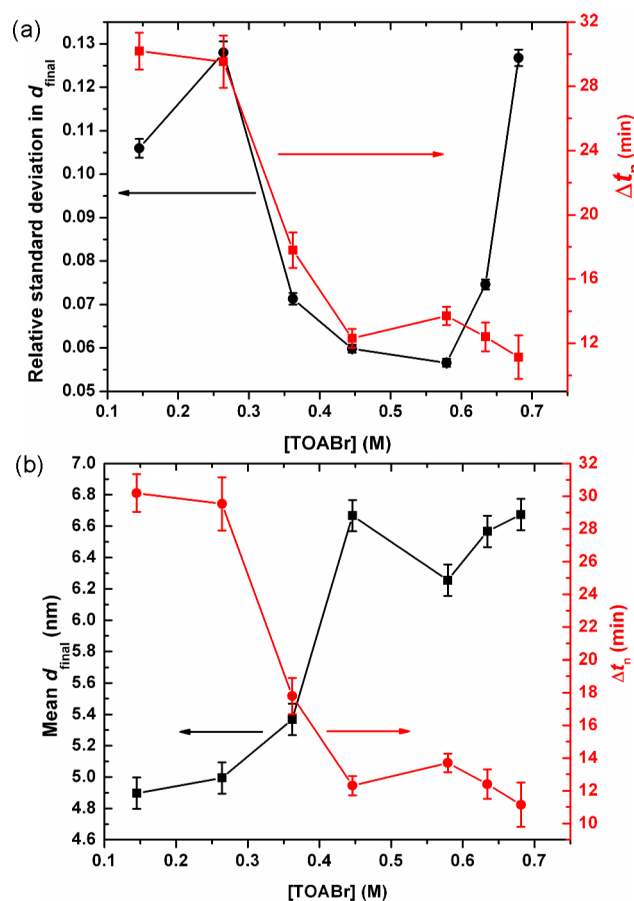

Figure 14. (a) Plots of the relative standard deviation in the final gold nanocrystal diameter distribution (black circles, left axis) and the time window for nucleation Δt_n (red squares, right axis) versus TOABr concentration. (b) Plots of the final gold nanocrystal mean diameter (black squares, left axis) and Δt_n (red circles, right axis) versus TOABr concentration. Reprinted with permission from ref 92. Copyright 2010, American Chemical Society, Washington, DC.

functions, presented in Figure 15, responded almost oppositely to added salt concentration as did those in Figure 12. In Figure 15, Δt_n and τ_n varied over small ranges, while Γ_{max} initially
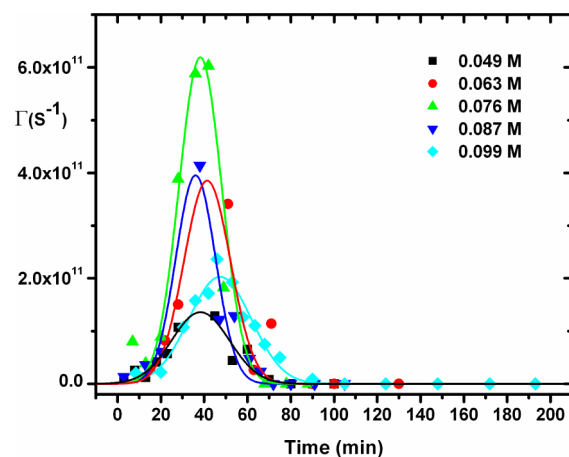

Figure 15. Nucleation functions for the synthesis of bismuth nanocrystals conducted at various concentrations of Na[N(SiMe$_3$)$_2$]. Reprinted with permission from ref 95. Copyright 2011, American Chemical Society, Washington, DC.

increased, and then decreased with increasing Na[N(SiMe₃)₂] concentration.

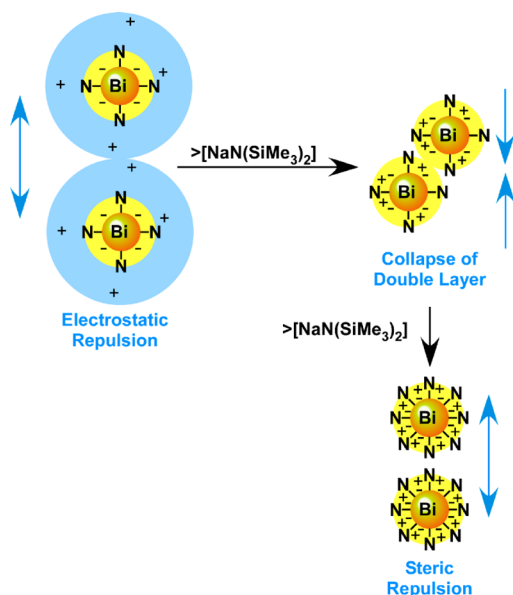The results were interpreted by adapting the electrical double-layer model described above (see Figure 16). We

Figure 16. Schematic depiction of the proposed roles of Na[N-(SiMe₃)₂] in the promotion and inhibition of aggregative nucleation of bismuth nanocrystals. The yellow region surrounding the bismuth nanocrystal core represents the polymer coating, and the light-blue region represents the double-layer (the extent of the Na^+ counterion atmosphere). The Na^+ ions are depicted by plus signs, and the [N(SiMe₃)₂]⁻ ligands attached to the bismuth surfaces are depicted by minus signs and N symbols. Reprinted with permission from ref 95. Copyright 2011, American Chemical Society, Washington, DC.

proposed that the initial increases in the added-salt concentration collapsed the double layer, as observed in the previous case, leading to decreased electrostatic stabilization and increasing nucleation rates, as reflected in the increasing Γ_{max} values. We noted that the added salt anion [N(SiMe₃)₂]⁻ may also serve as a surface ligand, and we speculated that the later increases in added-salt concentration decreased Γ_{max} by increasing the steric stabilization of the primary bismuth nanocrystals.

The nucleation parameters extracted from the Figure 15 nucleation functions exerted the expected influences on the final nanoparticle mean sizes and size distributions. As noted above, the final size dispersity was determined by the width of the nucleation period, and so Δt_n and the relative standard deviation in the final diameter distribution tracked each other (see Figure 17a). Because Δt_n was comparatively insensitive to Na[N(SiMe₃)₂] concentration, N was predominantly determined by Γ_{max}. Thus, Γ_{max} and the final mean size were anticorrelated as explained above (see Figure 17b).

The results demonstrated a primitive form of nucleation control: systematic changes in nucleation functions induced systematic changes in the final nanoparticle sizes and size distributions. The strong correlations between the nucleation parameters extracted from the nucleation functions and the final outcomes of the growth trials provides compelling support for considering the initiation of aggregative growth to be a nucleation-like event (see subsection 4.4).
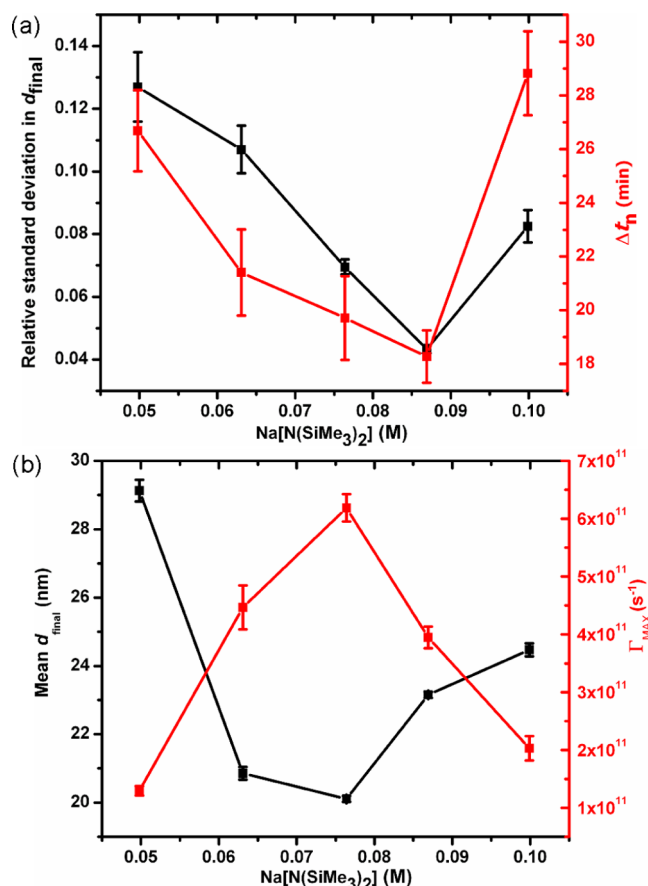

Figure 17. (a) Plots of the relative standard deviation in the final bismuth nanocrystal diameter distribution (black circles, left axis) and the time window for nucleation Δt_n (red squares, right axis) vs Na[N(SiMe₃)₂] concentration. (b) Plots of the final bismuth nanocrystal mean diameter (black squares, left axis) and the maximum nucleation rate Γ_{max} (red squares, right axis) vs Na[N(SiMe₃)₂] concentration. Reprinted with permission from ref 95. Copyright 2011, American Chemical Society, Washington, DC.

The nucleation control exhibited for the aggregative growth of bismuth nanocrystals is closer to the ideal situation in that Δt_n remained comparatively small, ensuring a narrow final size distribution, whereas variations in Γ_{max} controlled the final nanocrystal size. Unfortunately, we do not yet understand why the salt additive primarily influences Δt_n for gold-nanocrystal growth, but Γ_{max} for bismuth nanocrystal growth. The limited results currently available do not distinguish precisely how the additives separately affect Δt_n and Γ_{max}. Furthermore, we have not yet investigated how the other conditions (listed above) that influence colloidal stability may influence aggregative-nucleation functions. Rational nucleation control in nanocrystal synthesis will finally be achieved when Δt_n and Γ_{max} can be varied separately and purposefully.

6. SUMMARY AND OUTLOOK

Our goal in this review is to increase the awareness and appreciation of aggregative growth as a mechanism that may contribute to nanocrystal formation. We believe its synthetic potential remains largely untapped, and we hope to encourage further work in this area. As detailed herein, exciting recent advances in TEM techniques have now allowed aggregative nanocrystal growth and oriented attachment to be directly observed. Methods for collecting and analyzing kinetic data for

nanocrystal growth have also advanced rapidly. A variety of kinetic and mechanistic models for aggregative growth and oriented attachment have recently emerged. Aggregative growth is now understood to contribute to many, but not all,[12−18] nanocrystal-growth processes.

The great synthetic potential for aggregative growth is that the nucleation process may be measured and manipulated. The size and time scales for aggregative nucleation permit it to be observed, and conditions influencing colloidal stability allow its parameters to be systematically varied. Nucleation functions in aggregative growth have now been shown to determine nanocrystal sizes and size distributions.[92,94,95] Much remains to be learned about controlling the nucleation function, which is the key to nucleation control. The achievement of true nucleation control in aggregative growth will provide a firm mechanistic basis for size control in nanocrystal synthesis.

■ AUTHOR INFORMATION

Corresponding Author
*E-mail addresses: fwang@wustl.edu (F.W.), buhro@wustl.edu (W.E.B.).

Notes
The authors declare no competing financial interest.

■ ACKNOWLEDGMENTS

■ REFERENCES

(1) Hughes, E. D.; Ingold, C. K. *Nature* **1933**, *132*, 933−934.
(2) Gleave, J. L.; Hughes, E. D.; Ingold, C. K. *J. Chem. Soc.* **1935**, 236−244.
(3) Ingold, C. K. *J. Chem. Soc.* **1933**, 1120−1127.
(4) Melander, L. *Ark. Kemi* **1950**, *2*, 211−292.
(5) Shoppee, C. W. *Biogr. Mem. Fellows R. Soc.* **1972**, *18*, 349−411.
(6) Barton, D. H. R. *Bull. Hist. Chem.* **1996**, *19*, 43−47.
(7) Shakespeare, W. In *Macbeth*, Act IV, Scene I, Lines 14−15.
(8) Reiss, H. *J. Chem. Phys.* **1951**, *19*, 482−487.
(9) LaMer, V. K. *Ind. Eng. Chem.* **1952**, *44*, 1270−1277.
(10) LaMer, V. K.; Dinegar, R. H. *J. Am. Chem. Soc.* **1950**, *72*, 4847−4854.
(11) Sugimoto, T. *Adv. Colloid Interface Sci.* **1987**, *28*, 65−108.
(12) Murray, C. B.; Norris, D. J.; Bawendi, M. G. *J. Am. Chem. Soc.* **1993**, *115*, 8706−8715.
(13) Owen, J. S.; Chan, E. M.; Liu, H.; Alivisatos, A. P. *J. Am. Chem. Soc.* **2010**, *132*, 18206−18213.
(14) Morales, M. P.; Gonzalezcarreno, T.; Serna, C. J. *J. Mater. Res.* **1992**, *7*, 2538−2545.
(15) Saunders, A. E.; Sigman, M. B.; Korgel, B. A. *J. Phys. Chem. B* **2004**, *108*, 193−199.
(16) Robb, D. T.; Privman, V. *Langmuir* **2008**, *24*, 26−35.
(17) Drofenik, M.; Kristl, M.; Znidarsic, A.; Hanzel, D.; Lisjak, D. *J. Am. Ceram. Soc.* **2007**, *90*, 2057−2061.
(18) Bullen, C. R.; Mulvaney, P. *Nano Lett.* **2004**, *4*, 2303−2307.
(19) Wagner, C. *Z. Elektrochem.* **1961**, *65*, 581−591.
(20) Lifshitz, I. M.; Slyozov, V. V. *J. Phys. Chem. Solids* **1961**, *19*, 35−50.
(21) Meli, L.; Green, P. F. *ACS Nano* **2008**, *2*, 1305−1312.
(22) Lee, D.-K.; Park, S.-I.; Lee, J. K.; Hwang, N.-M. *Acta Mater.* **2007**, *55*, 5281−5288.
(23) Chen, Y.; Johnson, E.; Peng, X. *J. Am. Chem. Soc.* **2007**, *129*, 10937−10947.
(24) Jana, N. R.; Peng, X. G. *J. Am. Chem. Soc.* **2003**, *125*, 14280−14281.
(25) Ji, X.; Song, X.; Li, J.; Bai, Y.; Yang, W.; Peng, X. *J. Am. Chem. Soc.* **2007**, *129*, 13939−13948.
(26) Peng, X.; Wickham, J.; Alivisatos, A. P. *J. Am. Chem. Soc.* **1998**, *120*, 5343−5344.
(27) Stoeva, S.; Klabunde, K. J.; Sorensen, C. M.; Dragieva, I. *J. Am. Chem. Soc.* **2002**, *124*, 2305−2311.
(28) Thessing, J.; Qian, J.; Chen, H.; Pradhan, N.; Peng, X. *J. Am. Chem. Soc.* **2007**, *129*, 2736−2737.
(29) Zheng, N.; Fan, J.; Stucky, G. D. *J. Am. Chem. Soc.* **2006**, *128*, 6550−6551.
(30) Lin, X. M.; Sorensen, C. M.; Klabunde, K. J. *J. Nanoparticle Res.* **2000**, *2*, 157−164.
(31) Talapin, D. V.; Rogach, A. L.; Haase, M.; Weller, H. *J. Phys. Chem. B* **2001**, *105*, 12278−12285.
(32) Zhao, L.; Ji, X.; Sun, X.; Li, J.; Yang, W.; Peng, X. *J. Phys. Chem. C* **2009**, *113*, 16645−16651.
(33) Luo, Y. *Mater. Lett.* **2007**, *61*, 1039−1041.
(34) Qu, L.; Yu, W. W.; Peng, X. *Nano Lett.* **2004**, *4*, 465−469.
(35) Turkevich, J.; Stevenson, P. C.; Hillier, J. *Discuss. Faraday Soc.* **1951**, *11*, 55−75.
(36) Chow, M. K.; Zukoski, C. F. *J. Colloid Interface Sci.* **1994**, *165*, 97−109.
(37) Kwon, S. G.; Hyeon, T. *Acc. Chem. Res.* **2008**, *41*, 1696−1709.
(38) Abe, S.; Capek, R. K.; De Geyter, B.; Hens, Z. *ACS Nano* **2012**, *6*, 42−53.
(39) Kwon, S. G.; Piao, Y.; Park, J.; Angappane, S.; Jo, Y.; Hwang, N.-M.; Park, J.-G.; Hyeon, T. *J. Am. Chem. Soc.* **2007**, *129*, 12571−12584.
(40) Clark, M. D.; Kumar, S. K.; Owen, J. S.; Chan, E. M. *Nano Lett.* **2011**, *11*, 1976−1980.
(41) Widegren, J. A.; Aiken, J. D.; Ozkar, S.; Finke, R. G. *Chem. Mater.* **2001**, *13*, 312−324.
(42) Aiken, J. D.; Finke, R. G. *J. Am. Chem. Soc.* **1998**, *120*, 9545−9554.
(43) Watzky, M. A.; Finke, R. G. *J. Am. Chem. Soc.* **1997**, *119*, 10382−10400.
(44) Zheng, H.; Smith, R. K.; Jun, Y.-w.; Kisielowski, C.; Dahmen, U.; Alivisatos, A. P. *Science* **2009**, *324*, 1309−1312.
(45) Besson, C.; Finney, E. E.; Finke, R. G. *Chem. Mater.* **2005**, *17*, 4925−4938.
(46) Finney, E. E.; Finke, R. G. *Chem. Mater.* **2008**, *20*, 1956−1970.
(47) Hornstein, B. J.; Finke, R. G. *Chem. Mater.* **2004**, *16*, 139−150.
(48) Matijevic, E. *Chem. Mater.* **1993**, *5*, 412−426.
(49) Ott, L. S.; Finke, R. G. *Chem. Mater.* **2008**, *20*, 2592−2601.
(50) Besson, C.; Finney, E. E.; Finke, R. G. *J. Am. Chem. Soc.* **2005**, *127*, 8179−8184.
(51) Privman, V.; Goia, D. V.; Park, J.; Matijevic, E. *J. Colloid Interface Sci.* **1999**, *213*, 36−45.
(52) Kumar, S.; Davis, T. M.; Ramanan, H.; Penn, R. L.; Tsapatsis, M. *J. Phys. Chem. B* **2007**, *111*, 3398−3403.
(53) Libert, S.; Gorshkov, V.; Goia, D.; Matijevkic, E.; Privman, V. *Langmuir* **2003**, *19*, 10679−10683.
(54) Look, J. L.; Bogush, G. H.; Zukoski, C. F. *Faraday Discuss. Chem. Soc.* **1990**, *90*, 345−357.
(55) Bogush, G. H.; Zukoski, C. F. *J. Colloid Interface Sci.* **1991**, *142*, 19−34.
(56) Penn, R. L. *J. Phys. Chem. B* **2004**, *108*, 12707−12712.
(57) Van Hyning, D. L.; Klemperer, W. G.; Zukoski, C. F. *Langmuir* **2001**, *17*, 3128−3135.
(58) Penn, R. L.; Banfield, J. F. *Science* **1998**, *281*, 969−971.
(59) Penn, R. L.; Banfield, J. F. *Geochim. Cosmochim. Acta* **1999**, *63*, 1549−1557.
(60) Huang, F.; Zhang, H. Z.; Banfield, J. F. *Nano Lett.* **2003**, *3*, 373−378.

(61) Polte, J.; Erler, R.; Thunemann, A. F.; Sokolov, S.; Ahner, T. T.; Rademann, K.; Emmerling, F.; Kraehnert, R. *ACS Nano* **2010**, *4*, 1076−1082.

(62) Polte, J.; Tuaev, X.; Wuithschick, M.; Fischer, A.; Thuenemann, A. F.; Rademann, K.; Kraehnert, R.; Emmerling, F. *ACS Nano* **2012**, *6*, 5791−5802.

(63) Finney, E. E.; Shields, S. P.; Buhro, W. E.; Finke, R. G. *Chem. Mater.* **2012**, *24*, 1718−1725.

(64) Zhang, J.; Wang, Y.; Zheng, J.; Huang, F.; Chen, D.; Lan, Y.; Ren, G.; Lin, Z.; Wang, C. *J. Phys. Chem. B* **2007**, *111*, 1449−1454.

(65) Ustarroz, J.; Ke, X. X.; Hubin, A.; Bals, S.; Terryn, H. *J. Phys. Chem. C* **2012**, *116*, 2322−2329.

(66) Harada, M.; Kamigaito, Y. *Langmuir* **2012**, *28*, 2415−2428.

(67) Njoki, P. N.; Luo, J.; Kamundi, M. M.; Lim, S.; Zhong, C. J. *Langmuir* **2010**, *26*, 13622−13629.

(68) Yu, K.; Ouyang, J.; Leek, D. M. *Small* **2011**, *7*, 2250−2262.

(69) Xie, R.; Li, Z.; Peng, X. *J. Am. Chem. Soc.* **2009**, *131*, 15457−15466.

(70) Biswas, K.; Varghese, N.; Rao, C. N. R. *Small* **2008**, *4*, 649−655.

(71) Rempel, J. Y.; Bawendi, M. G.; Jensen, K. F. *J. Am. Chem. Soc.* **2009**, *131*, 4479−4489.

(72) Park, J.; Privman, V.; Matijevic, E. *J. Phys. Chem. B* **2001**, *105*, 11630−11635.

(73) van Embden, J.; Sader, J. E.; Davidson, M.; Mulvaney, P. *J. Phys. Chem. C* **2009**, *113*, 16342−16355.

(74) Gorshkov, V.; Privman, V. *Physica E* **2010**, *43*, 1−12.

(75) Daniel, T. R.; Ionel, H.; Vladimir, P.; Dan, V. G. *J. Chem. Phys.* **2008**, *129*, 184705.

(76) Skrdla, P. J. *Cryst. Growth Des.* **2011**, *11*, 1957−1965.

(77) Skrdla, P. J. *Langmuir* **2012**, *28*, 4842−4857.

(78) Skrdla, P. J. *J. Phys. Chem. C* **2012**, *116*, 214−225.

(79) Dixit, N. M.; Zukoski, C. F. *Phys. Rev. E* **2002**, *66*, 051602.

(80) Anwar, J.; Zahn, D. *Angew. Chem., Int. Ed.* **2011**, *50*, 1996−2013.

(81) Uyeda, N.; Nishino, M.; Suito, E. *J. Colloid Interface Sci.* **1973**, *43*, 264−276.

(82) Levit, A. B.; Rowell, R. L. *J. Colloid Interface Sci.* **1975**, *50*, 162−169.

(83) Murphy, P. J.; Posner, A. M.; Quirk, J. P. *J. Colloid Interface Sci.* **1976**, *56*, 270−283.

(84) Tang, Z.; Kotov, N. A.; Giersig, M. *Science* **2002**, *297*, 237−240.

(85) Chai, J.; Liao, X.; Giam, L. R.; Mirkin, C. A. *J. Am. Chem. Soc.* **2012**, *134*, 158−161.

(86) Evans, J. E.; Jungjohann, K. L.; Browning, N. D.; Arslan, I. *Nano Lett.* **2011**, *11*, 2809−2813.

(87) Parent, L. R.; Robinson, D. B.; Woehl, T. J.; Ristenpart, W. D.; Evans, J. E.; Browning, N. D.; Arslan, I. *ACS Nano* **2012**, *6*, 3589−3596.

(88) Xin, H. L. L.; Zheng, H. M. *Nano Lett.* **2012**, *12*, 1470−1474.

(89) Yuk, J. M.; Park, J.; Ercius, P.; Kim, K.; Hellebusch, D. J.; Crommie, M. F.; Lee, J. Y.; Zettl, A.; Alivisatos, A. P. *Science* **2012**, *336*, 61−64.

(90) Liao, H. G.; Cui, L. K.; Whitelam, S.; Zheng, H. M. *Science* **2012**, *336*, 1011−1014.

(91) Wette, P.; Schope, H. J.; Palberg, T. *J. Chem. Phys.* **2005**, *123*, 174902.

(92) Shields, S. P.; Richards, V. N.; Buhro, W. E. *Chem. Mater.* **2010**, *22*, 3212−3225.

(93) Ben-Eliyahu, Y.; Brill, M.; Mintz, M. H. *J. Chem. Phys.* **1999**, *111*, 6053−6060.

(94) Richards, V. N.; Rath, N. P.; Buhro, W. E. *Chem. Mater.* **2010**, *22*, 3556−3567.

(95) Richards, V. N.; Shields, S. P.; Buhro, W. E. *Chem. Mater.* **2011**, *23*, 137−144.

(96) Herlach, D. M.; Klassen, I.; Wette, P.; Holland-Moritz, D. *J. Phys.—Condens. Matter* **2010**, *22*, 153101.

(97) Wette, P.; Engelbrecht, A.; Salh, R.; Klassen, I.; Menke, D.; Herlach, D. M.; Roth, S. V.; Schope, H. J. *J. Phys.—Condens. Matter* **2009**, *21*, 464115.

(98) Wette, P.; Schope, H. J. *Phys. Rev. E* **2007**, *75*, 051405.

(99) Gualtieri, A. F. *Phys. Chem. Miner.* **2001**, *28*, 719−728.

(100) Gasser, U.; Weeks, E. R.; Schofield, A.; Pusey, P. N.; Weitz, D. A. *Science* **2001**, *292*, 258−262.

(101) Watzky, M. A.; Finney, E. E.; Finke, R. G. *J. Am. Chem. Soc.* **2008**, *130*, 11959−11969.

(102) Liu, J.; Nicholson, C. E.; Cooper, S. J. *Langmuir* **2007**, *23*, 7286−7292.

(103) Bryan, J. D.; Schwartz, D. A.; Gamelin, D. R. *J. Nanosci. Nanotech.* **2005**, *5*, 1472−1479.

(104) Rauscher, H.; Braun, J.; Behm, R. J. *Phys. Rev. Lett.* **2006**, *96*, 116101.

(105) Tobler, D. J.; Shaw, S.; Benning, L. G. *Geochim. Cosmochim. Acta* **2009**, *73*, 5377−5393.

(106) Anisimov, M. P.; Cherevko, A. G. *J. Aerosol Sci.* **1985**, *16*, 97−107.

(107) Wagner, W. *J. Phys. F: Met. Phys.* **1986**, *16*, L239−L243.

(108) Conrad, C. F.; Icopini, G. A.; Yasuhara, H.; Bandstra, J. Z.; Brantley, S. L.; Heaney, P. J. *Geochim. Cosmochim. Acta* **2007**, *71*, 531−542.

(109) Leyssale, J.-M.; Delhommelle, J.; Millot, C. *J. Chem. Phys.* **2007**, *127*, 044504.

(110) Yau, S. T.; Vekilov, P. G. *J. Am. Chem. Soc.* **2001**, *123*, 1080−1089.

(111) Galkin, O.; Vekilov, P. G. *J. Cryst. Growth* **2001**, *232*, 63−76.

(112) Malkin, A. J.; McPherson, A. *J. Cryst. Growth* **1993**, *128*, 1232−1235.

(113) Malkin, A. J.; McPherson, A. *Acta Crystallogr., Sect. D: Biol. Crystallogr.* **1994**, *50*, 385−395.

(114) Gersh, O. B.; Eli, R. *J. Chem. Phys.* **2002**, *117*, 7732−7737.

(115) Hou, Z.-Y.; Liu, R.-S.; Liu, H.-R.; Tian, Z.-A.; Wang, X.; Zhou, Q.-Y.; Chen, Z.-H. *J. Chem. Phys.* **2007**, *127*, 174503.

(116) Ong, W. J.; Tok, E. S. *Phys. Chem. Chem. Phys.* **2007**, *9*, 991−995.

(117) Grogan, J. M.; Rotkina, L.; Bau, H. H. *Phys. Rev. E* **2011**, *83*.

(118) Williamson, M. J.; Tromp, R. M.; Vereecken, P. M.; Hull, R.; Ross, F. M. *Nat. Mater.* **2003**, *2*, 532−536.

(119) Witten, T. A., Jr.; Sander, L. M. *Phys. Rev. Lett.* **1981**, *47*, 1400−1403.

(120) Witten, T. A.; Sander, L. M. *Phys. Rev. B* **1983**, *27*, 5686−5697.

(121) Kolb, M.; Botet, R.; Jullien, R. *Phys. Rev. Lett.* **1983**, *51*, 1123−1126.

(122) Meakin, P. *Phys. Rev. Lett.* **1983**, *51*, 1119−1122.

(123) Lin, M. Y.; Lindsay, H. M.; Weitz, D. A.; Klein, R.; Ball, R. C.; Meakin, P. *J. Phys.: Condens. Matter* **1990**, *2*, 3093−3113.

(124) Meakin, P. *Phys. Rev. A* **1983**, *27*, 604−607.

(125) Kolb, M.; Jullien, R. *J. Phys., Lett.* **1984**, *45*, 977−981.

(126) Jullien, R.; Kolb, M. *J. Phys. A: Math. Gen.* **1984**, *17*, L639−L643.

(127) Brown, W. D.; Ball, R. C. *J. Phys. A: Math. Gen.* **1985**, *18*, L517−L512.

(128) Weitz, D. A.; Huang, J. S.; Lin, M. Y.; Sung, J. *Phys. Rev. Lett.* **1985**, *54*, 1416−1419.

(129) Weitz, D. A.; Lin, M. Y. *Phys. Rev. Lett.* **1986**, *57*, 2037−2040.

(130) Ball, R. C.; Weitz, D. A.; Witten, T. A.; Leyvraz, F. *Phys. Rev. Lett.* **1987**, *58*, 274−277.

(131) Lin, M. Y.; Lindsay, H. M.; Weitz, D. A.; Ball, R. C.; Klein, R.; Meakin, P. *Phys. Rev. A* **1990**, *41*, 2005−2020.

(132) Smoluchowski, M. *Phys. Z.* **1916**, *17*, 557−585.

(133) Davis, T. M.; Drews, T. O.; Ramanan, H.; He, C.; Dong, J.; Schnablegger, H.; Katsoulakis, M. A.; Kokkoli, E.; McCormick, A. V.; Penn, R. L.; Tsapatsis, M. *Nat. Mater.* **2006**, *5*, 400−408.

(134) Huang, F.; Zhang, H.; Banfield, J. F. *J. Phys. Chem. B* **2003**, *107*, 10470−10475.

(135) Zhang, J.; Lin, Z.; Lan, Y.; Ren, G.; Chen, D.; Huang, F.; Hong, M. *J. Am. Chem. Soc.* **2006**, *128*, 12981−12987.

(136) Zhuang, Z.; Zhang, J.; Huang, F.; Wang, Y.; Lin, Z. *Phys. Chem. Chem. Phys.* **2009**, *11*, 8516−8521.

(137) Maye, M. M.; Zheng, W. X.; Leibowitz, F. L.; Ly, N. K.; Zhong, C. J. *Langmuir* **2000**, *16*, 490−497.

(138) Maye, M. M.; Zhong, C. J. *J. Mater. Chem.* **2000**, *10*, 1895−1901.

(139) Prakash, A.; Bapat, A. P.; Zachariah, M. R. *Aerosol Sci. Technol.* **2003**, *37*, 892−898.

(140) Gusak, A. M.; Hodaj, F.; Bogatyrev, A. O. *J. Phys.: Condens. Matter* **2001**, *13*, 2767−2787.

(141) Talukdar, S. S.; Swihart, M. T. *J. Aerosol Sci.* **2004**, *35*, 889−908.

(142) Lummen, N.; Kraska, T. *J. Aerosol Sci.* **2005**, *36*, 1409−1426.

(143) Mukherjee, D.; Prakash, A.; Zachariah, M. R. *J. Aerosol Sci.* **2006**, *37*, 1388−1399.

(144) Wachi, S.; Jones, A. G. *Chem. Eng. Sci.* **1992**, *47*, 3145−3148.

(145) Halfon, A.; Kaliaguine, S. *Can. J. Chem. Eng.* **1976**, *54*, 168−172.

(146) Budz, J.; Jones, A. G.; Mullin, J. W. *J. Chem. Technol. Biotechnol.* **1986**, *36*, 153−161.

(147) Xiong, Y.; Pratsinis, S. E. *J. Aerosol Sci.* **1991**, *22*, 637−655.

(148) Hostomsky, J.; Jones, A. G. *J. Phys. D: Appl. Phys.* **1991**, *24*, 165−170.

(149) Eberl, D. D.; Drits, V. A.; Srodon, J. *Am. J. Sci.* **1998**, *298*, 499−533.

(150) Park, K. S.; Lee, B. W.; Choi, M. *Aerosol Sci. Technol.* **1999**, *31*, 258−274.

(151) Carlow, G. R. *Physica A* **1997**, *239*, 65−77.

(152) Seto, T.; Shimada, M.; Okuyama, K. *Aerosol Sci. Technol.* **1995**, *23*, 183−200.

(153) Beckman, J. R.; Farmer, R. W. *AIChE Symp. Ser.* **1987**, *83*, 85−94.

(154) Madras, G.; McCoy, B. J. *J. Colloid Interface Sci.* **2003**, *261*, 423−433.

(155) Mantzaris, N. V. *Chem. Eng. Sci.* **2005**, *60*, 4749−4770.

(156) Datye, A. K.; Xu, Q.; Kharas, K. C.; McCarty, J. M. *Catal. Today* **2006**, *111*, 59−67.

(157) Voorhees, P. W. *Annu. Rev. Mater. Sci.* **1992**, *22*, 197−215.

(158) Zheng, X. *Z. Phys. B* **1994**, *93*, 501−507.

(159) Turkevich, J. *Gold Bull.* **1985**, *18*, 86−91.

(160) Callister, W. D. *Materials Science and Engineering: An Introduction*, 3rd Edition; John Wiley & Sons, Inc.: New York, 1994.

(161) Burbelko, A. A.; Fras, E.; Kapturkiewicz, W. *Mater. Sci. Eng., A* **2005**, *413−414*, 429−434.

(162) Christian, J. W. *The Theory of Transformation in Metals and Alloys*, 2nd Edition; Pergamon Press: Oxford, U.K., 1981; p 542.

(163) Levine, L. E.; Narayan, K. L.; Kelton, K. F. *J. Mater. Res.* **1997**, *12*, 124−132.

(164) Norby, P. *J. Am. Chem. Soc.* **1997**, *119*, 5215−5221.

(165) Price, F. P.; Wendorff, J. H. *J. Phys. Chem.* **1971**, *75*, 2839−2849.

(166) Yang, C. P.; Nagle, J. F. *Phys. Rev. A* **1988**, *37*, 3993−4000.

(167) van Osdol, W. W.; Ye, Q.; Johnson, M. L.; Biltonen, R. L. *Biophys. J.* **1992**, *63*, 1011−1017.

(168) Di Lorenzo, M. L.; Silvestre, C. *Prog. Polym. Sci.* **1999**, *24*, 917−950.

(169) Yang, J.; McCoy, B. J.; Madras, G. *J. Chem. Phys.* **2005**, *122*, 064901.

(170) Egan, T. J.; Tshivhase, M. G. *Dalton Trans.* **2006**, 5024−5032.

(171) Skrdla, P. J.; Robertsont, R. T. *Chem. Mater.* **2008**, *20*, 3−4.

(172) Typographical errors were unfortunately present in eq 1 (eq 3 in ref 92) and eq 13 (eq 6 in ref 94 and eq 1 in ref 95) in the primary literature, where $\exp(-k_g t)^n$ should have been written as $\exp\{-(k_g t)^n\}$.

(173) Avrami, M. *J. Chem. Phys.* **1939**, *7*, 1103−1112.

(174) Avrami, M. *J. Chem. Phys.* **1940**, *8*, 212−224.

(175) Avrami, M. *J. Chem. Phys.* **1941**, *9*, 177−184.

(176) Finney, E. E.; Finke, R. G. *Chem. Mater.* **2009**, *21*, 4692−4705.

(177) Derjaguin, B. L.; Landau, L. *Acta Physicochim. URSS* **1941**, *14*, 633−662.

(178) Verwey, E. J.; Overbeek, J.-T. G. *Theory of the Stability of Lyophobic Colloids*; Elsevier: Amsterdam, 1948.

(179) Stokes, R. J.; Evans, D. F. *Fundamentals of Interfacial Engineering*; VCH Publishers: New York, 1997.

(180) Lee Penn, R.; Tanaka, K.; Erbs, J. *J. Cryst. Growth* **2007**, *309*, 97−102.

(181) Burrows, N. D.; Hale, C. R. H.; Penn, R. L. *Cryst. Growth Des.* **2012**, *12*, 4787−4797.

(182) Skrdla, P. J. *J. Phys. Chem. A* **2009**, *113*, 9329−9336.

(183) Skrdla, P. J. *J. Phys. Chem. A* **2011**, *115*, 6413−6425.

(184) Van Hyning, D. L.; Zukoski, C. F. *Langmuir* **1998**, *14*, 7034−7046.

(185) Polte, J.; Ahner, T. T.; Delissen, F.; Sokolov, S.; Emmerling, F.; Thunemann, A. F.; Kraehnert, R. *J. Am. Chem. Soc.* **2010**, *132*, 1296−1301.

(186) Enustun, B. V.; Turkevich, J. *J. Am. Chem. Soc.* **1963**, *85*, 3317−3328.

(187) Takesue, M.; Tomura, T.; Yamada, M.; Hata, K.; Kuwamoto, S.; Yonezawa, T. *J. Am. Chem. Soc.* **2011**, *133*, 14164−14167.

(188) Wang, F.; Tang, R.; Yu, H.; Gibbons, P. C.; Buhro, W. E. *Chem. Mater.* **2008**, *20*, 3656−3662.

(189) Harada, M.; Katagiri, E. *Langmuir* **2010**, *26*, 17896−17905.

(190) Harada, M.; Tamura, N.; Takenaka, M. *J. Phys. Chem. C* **2011**, *115*, 14081−14092.

(191) Bhimalapuram, P.; Chakrabarty, S.; Bagchi, B. *Phys. Rev. Lett.* **2007**, *98*, 206104.

(192) Hassan, S. A. *J. Chem. Phys.* **2011**, *134*, 114508.

(193) ten Wolde, P. R.; Ruiz-Montero, M. J.; Frenkel, D. *Phys. Rev. Lett.* **1995**, *75*, 2714−2717.

(194) Khan, S. J.; Weaver, O. L.; Sorensen, C. M.; Chakrabarti, A. *Langmuir* **2012**, *28*, 16015−16021.

(195) Gebauer, D.; Colfen, H. *Nano Today* **2011**, *6*, 564−584.

(196) Drews, T. O.; Katsoulakis, M. A.; Tsapatsis, M. *J. Phys. Chem. B* **2005**, *109*, 23879−23887.

(197) Matijevic, E.; Goia, D. *Croatica Chem. Acta* **2007**, *80*, 485−491.

(198) Bogush, G. H.; Zukoski, C. F. *J. Colloid Interface Sci.* **1991**, *142*, 1−18.

(199) Hiramatsu, H.; Osterloh, F. E. *Chem. Mater.* **2004**, *16*, 2509−2511.

(200) Kasuya, A.; Sivamohan, R.; Barnakov, Y. A.; Dmitruk, I. M.; Nirasawa, T.; Romanyuk, V. R.; Kumar, V.; Mamykin, S. V.; Tohji, K.; Jeyadevan, B.; Shinoda, K.; Kudo, T.; Terasaki, O.; Liu, Z.; Belosludov, R. V.; Sundararajan, V.; Kawazoe, Y. *Nat. Mater.* **2004**, *3*, 99−102.

(201) Fojtik, A. W., H.; Koch, U.; Henglein, A. *Ber. Bunsen Ges. Phys. Chem.* **1984**, *88*, 969−977.

(202) Peng, Z. A.; Peng, X. *J. Am. Chem. Soc.* **2002**, *124*, 3343−3353.

(203) Soloviev, V. N.; Eichhofer, A.; Fenske, D.; Banin, U. *J. Am. Chem. Soc.* **2001**, *123*, 2354−2364.

(204) Cumberland, S. L.; Hanif, K. M.; Javier, A.; Khitrov, G. A.; Strouse, G. F.; Woessner, S. M.; Yun, C. S. *Chem. Mater.* **2002**, *14*, 1576−1584.

(205) Brust, M.; Walker, M.; Bethell, D.; Schiffrin, D. J.; Whyman, R. *J. Chem. Soc.−Chem. Commun* **1994**, 801−802.

(206) Waters, C. A.; Mills, A. J.; Johnson, K. A.; Schiffrin, D. J. *Chem. Commun.* **2003**, 540−541.

■ NOTE ADDED AFTER ASAP PUBLICATION

This article was published ASAP on September 12, 2013, with an error in eq 11. The corrected version was published ASAP on September 13, 2013.

21

dx.doi.org/10.1021/cm402139r | *Chem. Mater.* 2014, 26, 5−21